7922–7937 *Nucleic Acids Research, 2017, Vol. 45, No. 13* *Published online 27 June 2017*
doi: 10.1093/nar/gkx535

A new role for FBP21 as regulator of Brr2 helicase activity

Lisa M. Henning[1], Karine F. Santos[2], Jana Sticht[1,3], Stefanie Jehle[4], Chung-Tien Lee[5,6], Malte Wittwer[1], Henning Urlaub[5,6], Ulrich Stelzl[4], Markus C. Wahl[2,7,*] and Christian Freund[1,*]

[1]Laboratory of Protein Biochemistry, Institute for Chemistry and Biochemistry, Freie Universität Berlin, Thielallee 63, Berlin 14195, Germany, [2]Laboratory of Structural Biochemistry, Freie Universität Berlin, Takustr. 6, Berlin 14195, Germany, [3]BioSupraMol Gerätezentrum, Freie Universität Berlin, Takustr. 3, Berlin 14195, Germany, [4]Max-Planck-Insitute for Molecular Genetics, Ihnestraße 63–74, Berlin 14195, Germany, [5]Max-Planck-Institute for Biophysical Chemistry, Bioanalytical Mass Spectrometry Group, Am Fassberg 11, Göttingen 37077, Germany, [6]University Medical Center Goettingen, Bioanalytics, Department of Clinical Chemistry, Robert Koch Strasse 40, Göttingen 37075, Germany and [7]Helmholtz-Zentrum Berlin für Materialien und Energie, Macromolecular Crystallography, Albert- Einstein-Straße 15, Berlin 12489, Germany

Received February 10, 2017; Revised June 06, 2017; Editorial Decision June 07, 2017; Accepted June 19, 2017

ABSTRACT

Splicing of eukaryotic pre-mRNA is carried out by the spliceosome, which assembles stepwise on each splicing substrate. This requires the concerted action of snRNPs and non-snRNP accessory proteins, the functions of which are often not well understood. Of special interest are B complex factors that enter the spliceosome prior to catalytic activation and may alter splicing kinetics and splice site selection. One of these proteins is FBP21, for which we identified several spliceosomal binding partners in a yeast-two-hybrid screen, among them the RNA helicase Brr2. Biochemical and biophysical analyses revealed that an intrinsically disordered region of FBP21 binds to an extended surface of the C-terminal Sec63 unit of Brr2. Additional contacts in the C-terminal helicase cassette are required for allosteric inhibition of Brr2 helicase activity. Furthermore, the direct interaction between FBP21 and the U4/U6 di-snRNA was found to reduce the pool of unwound U4/U6 di-snRNA. Our results suggest FBP21 as a novel key player in the regulation of Brr2.

INTRODUCTION

The removal of non-coding introns from eukaryotic pre-mRNAs during pre-mRNA splicing is carried out by the spliceosome, a large molecular machine consisting of five small nuclear ribonucleoprotein particles (snRNPs, U1, U2, U4, U5 and U6 for the major spliceosome or U11, U12, U4atac, U5 and U6atac for the minor spliceosome) and a plethora of non-snRNP proteins. Unlike other macromolecular machines, the spliceosome assembles *de novo* for each splicing reaction in a step-wise manner. Firstly, the 5′ splice site, the 3′ splice site and branch point are defined, involving the sequential binding of U1 and U2 snRNPs (A complex). Recruitment of the U4/U6•U5 tri-snRNP then leads to the formation of the pre-catalytic B complex. Major compositional and conformational rearrangements through the action of spliceosomal helicases lead to a gradual activation of the spliceosome (B^{act} and B* complexes), which then carries out the two consecutive steps of the splicing reaction before it is disassembled and its components are recycled (1).

This description of the splicing cycle has been derived primarily from structural and functional studies of the spliceosome of *Saccharomyces cerevisiae*, which is a popular model organism due to its genetic tractability and relative simplicity. The core components of splicing are well conserved from yeast to human (2). However, while less than 5% of *S. cerevisiae* protein-coding genes contain introns (3,4), there are an average of 7.8 introns per gene in *Homo sapiens* (5–7) and human splice site and branch point sequences are more divergent. In addition, most human mRNAs undergo alternative splicing, which means that exons can be skipped, introns can be retained or alternative 5′ or 3′ splice sites can be used (8). Pervasive alternative splicing requires a higher level of regulation, which is also reflected in the larger number of spliceosomal proteins in higher eukary-

*To whom correspondence should be addressed. Tel: +49 30 838 51187; Fax: +49 30 838 56413; Email: chfreund@zedat.fu-berlin.de
Correspondence may also be addressed to Markus C. Wahl. Tel: +49 30 838 53456; Fax: +49 30 838 56981; Email: mwahl@zedat.fu-berlin.de
Present addresses:
Karine F. Santos, moloX GmbH, Takustr. 6, Berlin 14195, Germany.
Ulrich Stelzl, Institute of Pharmaceutical Sciences and BioTechMed-Graz, University of Graz, Universitätsplatz 1/I, Graz 8010, Austria.

otes (2). Equally, higher complexity gives room for dysregulation and disease (9) and splicing defects have been associated with inherited diseases, neurodegenerative diseases and cancer (10–12).

A group of proteins that may be of particular interest for splice site decisions are proteins that are present exclusively in the B complex (B complex-specific proteins), as they act directly before spliceosomal catalytic activation, which fixes the specific splicing pattern of a substrate through irreversible loss of U4 (13). In the transition from the B to the B^{act} complex, the RNA helicase Brr2 unwinds the U4/U6 duplex, releasing the U4 snRNP and enabling the U6 snRNA to base-pair with the U2 snRNA and to form a catalytically important stem–loop (14,15). It is thus a key player in spliceosomal activation.

Brr2 has a unique domain architecture, consisting of two similar helicase cassettes of which only the N-terminal cassette is catalytically active. Both helicase cassettes contain two RecA domains followed by a winged helix domain (WH) and a Sec63 unit, which is composed of a helical bundle (HB), a helix-loop-helix (HLH) and an immunoglobulin-like (IG) domain. In addition, Brr2 contains an approximately 450-residue N-terminal region ($Brr2^{NTR}$).

Brr2 already encounters the U4/U6 di-snRNP in the U4/U6•U5 tri-snRNP and remains associated with the spliceosome after catalytic activation (16–18). Thus, Brr2 is tightly regulated by various mechanisms for splicing to proceed in an ordered manner (19). Regulation of the helicase is achieved intramolecularly *via* the C-terminal cassette and *via* the $Brr2^{NTR}$ (16,17,20,21), which activate or inhibit the helicase, respectively. The C-terminal cassette interacts with the enzymatically active N-terminal cassette through a large interface (21), thereby acting as an intramolecular modulator of activity. The $Brr2^{NTR}$ contains several functional units implicated in inhibition of the helicase, which interact both with the N- and C-terminal helicase cassette (20).

Brr2 is additionally regulated by trans-acting factors, primarily by the C-terminal Jab1 domain of the spliceosomal Prp8 protein ($Prp8^{Jab1}$). Prp8 is the largest spliceosomal protein, which scaffolds the assembly of the catalytic core of the spliceosome (22,23). $Prp8^{Jab1}$ interacts with the Sec63 unit of the N-terminal cassette and can intermittently inhibit Brr2 by insertion of its intrinsically unstructured C-terminal tail into the Brr2 RNA-binding tunnel (24). In contrast, after removal of the tail, $Prp8^{Jab1}$ acts as a strong activator of the Brr2 helicase (24,25), an effect that is recapitulated by a C-terminally truncated version of the Jab1 domain ($Prp8^{Jab1\Delta C}$) (26).

The C-terminal helicase cassette has been postulated as a binding platform (27–29), but few interaction partners are known to date (28,30). Given the role of the C-terminal helicase cassette in regulating Brr2 activity it is of critical importance to identify proteins that bind to this region, thereby conceivably altering the kinetics of spliceosome activation *in trans*. B complex proteins would be particularly suitable to alter splicing fates by regulating Brr2 as they are present directly prior to Brr2 activity.

Of the eight B complex-specific proteins (Smu1, RED, MFAP1, FBP21, Snu23, Prp38, TFIP11 and Prp4-Kinase) (31), Smu1, RED, MFAP1 and FBP21 do not have an obvious *S. cerevisiae* homolog (31). Smu1, RED and MFAP1 have been studied structurally in context with other members of the B-complex (32–34). For Smu1 and RED, functional data is also available (32,35). However, little is known about the function of FBP21.

FBP21 contains two WW domains, for which an NMR structure is available (36). In addition, it is predicted to contain a matrin-type zinc finger in its N-terminal region (residues 11–42). The remainder of the protein appears to be intrinsically disordered. The tandem WW domains of FBP21 have been studied comprehensively. They interact with proline-rich sequence (PRS)-containing spliceosomal proteins such as SmB/B', SF3B4 and SIPP1 (36–38) and localize to nuclear speckles upon overexpression (36). Overexpression of FBP21 or its isolated tandem WW domains was shown to increase splicing efficiency of a reporter construct (36). In addition, FBP21 was suggested to modulate VEGF-A alternative splicing in the context of insulin-like growth factor 1 signaling (39).

FBP21 has no apparent catalytic activity, thus it likely fulfills its function by interaction with other spliceosomal components. The binding of all known interaction partners is mediated by WW domain-PRS interactions, which are typically of low affinity and high promiscuity (37) and thus barely yield information about FBP21's specific spliceosomal function. Therefore, we set out to identify molecules of the spliceosome interacting with FBP21 independent of its WW domains. Strikingly, we identified a novel interaction between FBP21 and the spliceosomal RNA helicase Brr2 and showed that FBP21 regulates the activity of the helicase.

MATERIALS AND METHODS

Yeast-two-hybrid assay

The yeast-two-hybrid assay was carried out as described previously (40) using the prey matrix established in (34). $FBP21^{FL}$ (1–376) and mutants $FBP21^{FL}$ W150A, $FBP21^{FL}$ W191A, $FBP21^{FL}$ W150A/W191A as well as the fragments $FBP21^{1\text{-}50}$, $FBP21^{1–200}$, $FBP21^{tWW}$ (117–200), $FBP21^{tWW}$ W29A, $FBP21^{tWW}$ W70A, $FBP21^{tWW}$ W29A/W70A, $FBP21^{tWW}$ Δlinker, $FBP21^{117–376}$, $FBP21^{117–376}$ W29A/W70A and $FBP21^{200–376}$ were cloned into pBTM-116-D9 and pBTM-CC24-DM vectors by Gateway cloning using standard procedures. Interacting bait-prey pairs were identified by growth on selective agar plates (lacking leucine, tryptophane, adenine, uracile and histidine). Growth was categorized into no growth (score = 0), weak growth (score = 1), medium growth (score = 2) and strong growth (score = 3). For each interacting protein the scores of all growing yeast spots were added to a final count. Only those pairs which showed a score of at least three were considered as a putative interaction. All bait constructs which were auto active and all prey constructs which had been previously shown to interact unspecifically were also not considered in the analysis.

Protein expression and purification

FBP21$^{200–376}$, FBP21$^{276–376}$, FBP21$^{326–376}$, FBP21$^{200–376}$ K357E/R359E, FBP21$^{200–376}$ K358A/R360A and FBP21$^{116–376}$ were expressed from pETM11 (EMBL, Heidelberg) vectors in *Escherichia coli* BL21-DE3 at 37°C for 4–4.5 h. Isotope-labeled proteins for NMR were produced in *E. coli* using M9 minimal medium, which was supplemented with amino acids for amino acid specific labeling and based on D_2O for protein deuteration. The pellet was resuspended in IMAC lysis buffer (50 mM KH_2PO_4, 300 mM KCl, 5 mM imidazole pH 8.0) supplemented with protease inhibitors (Roche) and lysed by sonication. The His-tagged proteins were subjected to affinity chromatography using a Ni-NTA column (Macherey-Nagel). During an overnight dialysis at 4°C to 10 mM Tris pH 8, 50 mM NaCl, the His-tag was removed by TEV protease. The cleaved protein was loaded on a Mono-Q 5/50 GL column (GE Healthcare) equilibrated with 10 mM Tris pH 8, 50 mM NaCl and eluted with a linear 50 to 1500 mM NaCl gradient and further purified by size exclusion chromatography using a HiLoad Superdex 75 column (GE Healthcare) in 10 mM Tris pH 7.5, 100 mM NaCl. Brr2$^{C\text{-}Sec63}$ was expressed from a pGEX6p vector in *E. coli* BL21-DE3 for 37°C for 4 h. The pellet was resuspended in GST lysis buffer (150 mM NaCl, 20 mM Na_2HPO_4, 10 mM EDTA pH 7.4) supplemented with protease inhibitors (Roche) and lysed by sonication. The GST-tagged proteins were subjected to affinity chromatography using a Glutathione 4B column (Macherey-Nagel). The eluted protein was subjected to size exclusion chromatography using a HiLoad Superdex 75 column (GE Healthcare) in 10 mM Tris pH 7.5, 100 mM NaCl. The GST-tag was cleaved using PreScission protease for 16 h at 4°C. The cleaved GST-tag, uncut protein and protease were removed by GST affinity chromatography and the target protein was further purified by size exclusion chromatography in 10 mM Tris, pH 7.5, 100 mM NaCl.

Brr2^{NC}, Brr2^{CC}, Brr2^{HR}, Brr2^{FL} were expressed in insect cells and purified as described (41). Briefly, High Five^{TM} cell pellets were resuspended in 50 mM HEPES-NaOH, pH 8.0, 600 mM NaCl, 2 mM β-mercaptoethanol, 0.05% NP40, 1.5 mM $MgCl_2$, 20% (v/v) glycerol, 10 mM imidazole, supplemented with EDTA-free protease inhibitor (Roche) and lyzed by sonication using a Sonopuls Ultrasonic Homogenizer HD 3100 (Bandelin). The target was captured from the cleared lysate on a 5 ml HisTrap FF column (GE Healthcare) and eluted with a linear gradient from 10 to 250 mM imidazole. The eluted protein was diluted to a final concentration of 80 mM NaCl, treated with RNaseA and loaded on a Mono Q 10/100 GL column (GE Healthcare) equilibrated with 50 mM Tris-HCl, pH 8.0, 50 mM NaCl, 5% (v/v) glycerol, 2 mM β-mercaptoethanol. The protein was eluted with a linear 0.05 to 1.5 M NaCl gradient and further purified by gel filtration on a 16/60 Superdex 200 gel filtration column (GE Healthcare) in 40 mM Tris–HCl, pH 8.0, 200 mM NaCl, 20% (v/v) glycerol, 2 mM DTT. The GST-tagged Prp8$^{Jab1\Delta C}$ was expressed in High Five^{TM} cells. Cell pellets were resuspended in binding buffer containing 50 mM Tris, pH 8.0, 300 mM NaCl, 5% (v/v) glycerol, 1 mM DTT, 0.05% NP40 supplemented with EDTA-free protease inhibitors and DNase I. The suspension was then lysed by sonication using a Sonopuls Ultrasonic Homogenizer HD 3100 (Bandelin), cell debris was removed by centrifugation and the soluble extract was filtered. The clear lysate was loaded onto GSH beads previously equilibrated with binding buffer and incubated 1 h at 4°C with gentle agitation. After washing the beads with 10 column volumes (CV) of binding buffer, the beads were incubated overnight with PreScission protease at 4°C. The cleaved protein was then collected as the flow through and the beads were washed with 2 CV of binding buffer to wash away all the cleaved protein from the beads. The flow through and wash fractions were collected, concentrated and loaded onto a S200 gelfiltration column equilibrated in Tris 10 mM pH 8.0, 150 mM NaCl and 1 mM DTT.

Cross-linking analysis

The primary amino group-reactive cross-linker BS3 (Pierce, Thermo Scientific) was used for cross-linking analysis. Brr2^{CC}, Brr2^{HR}, Brr2^{FL} were purified in complex with FBP21$^{200–376}$. 25 pmol of complex were cross-linked with 6 nmol BS3 in 20 mM HEPES–NaOH pH 7.3, 200 mM NaCl, 2 mM DTT and 5% (v/v) glycerol and incubated for 30 min at room temperature. The reaction was quenched with 1 μl of 1 M Tris–HCl. For Brr2^{CC}, the cross-linked sample was separated by SDS-PAGE, the band corresponding to the cross-linked complex was excised and the proteins were in-gel digested with trypsin. The peptides were dissolved in 5% acetonitrile and 0.1% formic acid for MS analysis. For Brr2^{FL} and Brr2^{HR}, the cross-linked complexes were pelleted by ultracentrifugation, dissolved in 4 M urea and 50 mM ammonium bicarbonate, reduced with DTT and alkylated with iodoacetamide. After dilution to 1 M urea, the complexes were digested with trypsin. Peptides were reverse-phase extracted and fractionated by size exclusion chromatography on a Superdex peptide PC3.2/300 column (GE Healthcare). Mass spectrometric analysis was performed on a Thermo Scientific Orbitrap Fusion Tribrid mass spectrometer coupled to a nano-LC system (UltiMate 3000 RSLCnano system). Protein-protein cross-links were identified by the pLink 1.22 search engine and filtered at FDR 1% (42). Cross-links which connected the N-terminal amino group of FBP21$^{200–376}$ to lysine residues of Brr2 were disregarded, as the N-terminus of FBP21$^{200–376}$ is artificial.

NMR spectroscopy

All NMR spectra were recorded on a Bruker Avance 700 MHz spectrometer equipped with a 5 mm triple resonance cryoprobe. Spectra were processed using TopSpin3.1 (Bruker) and analyzed using CCPNMR Analysis 2.2.2. (43). Triple resonance spectra (HNCA, HNCOCA, HNCO, HNCACO and ^{1}H–^{15}N-NOESY) for backbone assignments were recorded with ^{2}H–^{15}N-^{13}C-labeled Brr2$^{C\text{-}Sec63}$ at concentrations of 200–500 μM in 10 mM sodium phosphate pH 7.0, 100 mM NaCl supplemented with 10% D_2O at 300 K. Non-uniform sampling (25%) was used to reduce measurement time. Assignment of the HSQC signals was accomplished using CCPNMR Analysis 2.2.2 (43) and chemical shift predictions derived from the crystal structure of Brr2$^{C\text{-}Sec63}$ (part of PDB ID 4F91) using ShiftX2

(44). All ^{1}H–^{15}N-TROSY-HSQC spectra of amino acid-selectively labeled Brr2$^{C\text{-}Sec63}$ (Leu, Ala (-Trp), Ile, Val, Gly (–Ser, –Cys), Trp–Tyr, Tyr–Phe) were measured at 100–300 μM in 10 mM sodium phosphate pH 7.0, 100 mM NaCl supplemented with 10% D_2O at 300 K with 32–128 scans depending on the concentration and 1024 × 96 datapoints. All ^{1}H–^{15}N-TROSY-HSQC spectra of uniformly labeled proteins were measured at 100 μM in 10 mM Tris, 100 mM NaCl pH 7.5 supplemented with 10% D_2O at 300 K with 32 scans and 1024 × 96 datapoints. NMR spectra of ^{15}N-labeled FBP21$^{276–376}$ were measured at a concentration of 100 μM with a 2-fold excess of Brr2$^{C\text{-}Sec63}$. NMR spectra of ^{15}N-labeled Brr2$^{C\text{-}Sec63}$ were measured at a concentration of 100 μM with a two-fold excess of ligand (FBP21$^{276–376}$, FBP21$^{200–376}$ K357ER359E and FBP21$^{326–376}$ and FBP21$^{276–376}$), a four-fold excess of ligand (FBP21$^{276–376}$) or a seven-fold excess of ligand (peptide 57 GVMADGVAPVFKKRRTENGK and peptide 58 GVAPVFKKRRTENGKSRNLR). For the NMR titrations, spectra were acquired with 100 μM Brr2$^{C\text{-}Sec63}$ and 12.5, 25, 50, 75, 100, 150, 200 and 400 μM FBP21$^{276–376}$. Assignments of the unbound Brr2$^{C\text{-}Sec63}$ were transferred to the nearest neighbors of the bound state, employing amino-acid-type selectively-labeled Brr2$^{C\text{-}Sec63}$ in complex with FBP21$^{276–376}$ to help identifying longer shift distances. Chemical shift differences were calculated by $\{\Delta\delta^{1}H/^{15}N = SQRT((\delta^{1}H)^2 + (0.15*\delta^{15}N)^2\}$ and were considered to be strongly shifting when they exceeded the average plus standard deviation and weakly shifting when they exceeded the average chemical shift distance. The chemical shift changes were plotted on the structure using the PyMOL Molecular Graphics System, Version 1.8 Schrödinger, LLC. For soluble paramagnetic relaxation enhancement (PRE) experiments, Gadopentetic acid (Gd(DTPA)$^{2-}$) was used at 0, 2, 5 and 10 mM with Brr2$^{C\text{-}Sec63}$ alone or in complex with FBP21$^{276–376}$. All ^{1}H–^{15}N-TROSY-HSQC spectra for PRE experiments were recorded at 100 μM Brr2$^{C\text{-}Sec63}$ and 200 μM FBP21$^{276–376}$ (if applicable) in 10 mM Tris, 100 mM NaCl pH 7.5 supplemented with 10% D_2O at 300 K with 32 scans and 1024 × 96 datapoints. Peak intensities of all single assigned peaks were extracted using CCPNMR Analysis (43). To obtain a value for the intensity loss, the peak intensities of the Gd(DTPA)$^{2-}$-samples were divided by the peak intensities of the spectrum without Gd(DTPA)$^{2-}$, always with and without ligand. Subsequently, the intensity loss of each peak with ligand was subtracted from each peak without ligand. Values above the overall average difference plus standard deviation (0.33) were considered a strong protection from the PRE, values above the average difference (0.16) a weak protection. Likewise, values below the negative average difference minus standard deviation (−0.33) were considered a strong deprotection, values below the negative average difference (−0.16) a weak protection.

Peptide SPOT analysis

Peptide SPOT analyses were performed as described (38). Briefly, membranes were blocked with 5% BSA in 20 mM Tris pH 7.4, 150 mM NaCl, 2 mM DTT, washed and incubated with His-Brr2^{NC}, His-Brr2^{CC}, His-Brr2^{HR} or His-Brr2^{FL} at a concentration of 25 μg/ml (His-Brr2^{NC}, His-Brr2^{CC}), 50 μg/ml (His-Brr2^{HR}) or 60 μg/ml (His-Brr2^{FL}), respectively, overnight at 4°C. The SPOT arrays were washed and then incubated with an HRP-coupled anti-His antibody (Miltenyi Biotech) for 1 h at room temperature in blocking buffer and washed again. The Peptide Spot Arrays were developed with HRP juice purchased from p.j.k. GmbH on an Intas Advanced Fluorescence and ECL imager.

Isothermal titration calorimetry

All ITC experiments were carried out using a MicroCal ITC200 (Malvern) at 25°C. Where possible, both binding partners were dialyzed against the ITC buffer (10 mM Tris pH 7.5, 100 mM NaCl). Peptides were dissolved in ITC buffer and the pH was adjusted. For all experiments with Brr2$^{C\text{-}Sec63}$ and FBP21 fragments except peptide 58, Brr2$^{C\text{-}Sec63}$ was in the cell and the FBP21 ligand in the syringe. For ITC experiments with FBP21$^{200–376}$, FBP21$^{276–376}$ FBP21$^{326–376}$ and FBP21$^{116–376}$, Brr2$^{C\text{-}Sec63}$ was concentrated to 30 μM and the FBP21 fragment to 400 μM. For experiments with the peptides and FBP21 mutants, Brr2$^{C\text{-}Sec63}$ was concentrated to 50 μM, the peptide to 800 μM and the mutants to 600 μM. For experiments with Brr2C-Sec63 and peptide 58, peptide 58 used at 30 μM in the cell and Brr2C-Sec63 at a concentration of 400 μM in the syringe. For experiments with FBP21$^{116–376}$ and SmB-peptide, FBP21 was in the cell at a concentration of 100 μM and SmB-peptide in the syringe at a concentration of 2 mM. For experiments with all three components, either 400 μM FBP21$^{116–376}$ and 2 mM SmB peptide were pre-incubated together and used as a ligand for 30 μM Brr2$^{C\text{-}Sec63}$, or 100 μM Brr2$^{C\text{-}Sec63}$ and 100 μM FBP21$^{116–376}$ were pre-incubated and used with 2 mM SmB peptide as a ligand. In the control, 200 μM Brr2$^{C\text{-}Sec63}$ and 4 mM SmB peptide were used. The experiment started with one injection of 1 μl followed by 25 injections of 2 μl. The data was analyzed with Origin and the Microcal ITC 200 AddOn to obtain stoichiometry, association constant, reaction enthalpy and reaction entropy. The baseline was corrected, the first point was removed and the enthalpy of solvation was subtracted. The peak areas were integrated and reaction heats were plotted against the molar ratio of titrant versus analyte. The data was fitted with the model for one binding site using the Microcal ITC 200 Add-on in Origin.

Preparation of ^{32}P-labeled U4 and U4/U6 duplex snRNA

RNAs and duplexes were prepared as in (26). Briefly, U4 and U6 were produced by T7 RNA polymerase-based *in vitro* transcription. U4 was dephosphorylated and 5′ labeled using T4 polynucleotide kinase and $\gamma^{32}P$-ATP. For duplex preparation U4 was annealed with U6 and purified by native PAGE, PCI extraction and ethanol precipitation.

Electrophoretic mobility shift assays (EMSA)

1 nM ^{32}P-labeled U4/U6 duplex snRNA was titrated with increasing amounts of Brr2 alone or in presence of 600 nM or 5 μM FBP21$^{200–376}$ or FBP21$^{276–376}$ or FBP21 fragments alone in 40 mM HEPES–NaOH (pH 7.9), 15 mM NaCl, 2.5

mM NaOAc, 1 mM DTT and 0.1 mg/ml acetylated BSA in appropriate concentration ranges. Samples were separated by native PAGE using a 4% (75:1) gel for Brr2 and a 6% (19:1) gel for FBP21. Gels were scanned on a Storm PhosphorImager (GE Healthcare) and bands were quantified using ImageQuant software. Fitting the resulting data points to a single exponential Hill function {fraction bound = A[protein]^n/([protein]^n + K_D}, in which A is the fitted maximum of bound U4/U6 snRNA and n is the Hill coefficient} using GraphPad Prism yielded apparent K_D values.

Unwinding assays

Unwinding assays were performed as described (21,41). 100 nM Brr2 were incubated with 2 nM ^{32}P-labeled U4/U6 di-snRNA at 30°C in a buffer containing 40 mM Tris pH 7.5, 50 mM NaCl, 5 mM $MgCl_2$, 1.5 mM DTT, 0.1 mg/ml acetylated BSA, 8% (v/v) glycerol with or without FBP21. After addition of 1 mM ATP/$MgCl_2$, 10 μl of the reaction were taken and quenched with 10 μl stop buffer (40 mM Tris pH 7.4, 50 mM NaCl, 25 mM EDTA, 1% SDS, 10% (v/v) glycerol, 0.05% xylenecyanol and 0.05% bromophenol blue) at the respective time points. In addition, a sample was taken and boiled to fully disrupt the RNA duplex. The samples were separated by native PAGE using a 6% (19:1) gel. Gels were scanned on a Storm PhosphorImager (GE Healthcare). Quantification of the bands was carried out using the ImageQuant software. After background correction, band intensities were extracted and the percentage of unwound duplex is calculated and plotted over time and fitted with GraphPad Prism (GraphPad Software, Inc.) to a first-order reaction {U4/U6 snRNA unwound = A[1 − exp(−k_ut)], in which A is the amplitude of the reaction, k_u the apparent rate of unwinding and t is time}.

RESULTS

A yeast-two-hybrid screen identifies Brr2 as a binding partner of FBP21

In order to identify possible binding partners for FBP21 in the spliceosome, we conducted a yeast-two-hybrid (Y2H) screen against a spliceosomal matrix composed of 237 proteins represented by 442 clones of full length human spliceosomal proteins and fragments encompassing domains or predicted folding units (34). By using various fragments of FBP21 as well as mutants that prevented binding to PRS via one or both WW domains (W150A, W191A or W150A/W191A, respectively) as bait proteins (domain structure shown in Figure 1A), we identified 15 high-confidence binding partners (Table 1) and roughly mapped their interaction sites.

All bait constructs containing two intact WW domains or the intact WW2 domain were transcriptionally autoactivating. This prevented the identification of well-known interaction partners that bind FBP21 via PRS. Nevertheless, full-length FBP21 containing an intact WW1 domain interacted with numerous proteins, some of which contained proline-rich binding motifs (hnRNPK, ISY1, SIPP1, SF3A1, Prp16 and Prp43, Table 1). Some of these interaction partners (SF3A1, SIPP1, hnRNPK) were detected previously in pull-down approaches (36,37). More interestingly, we identified interaction partners independent of FBP21's WW domains. For several of those (MORG1, SKIP, PPIH, FAM164A and FAM50B), a binding region could not be derived, since they interacted only with full length constructs. TIA-1 and ARGLU-1, two proteins known to bind pre-mRNAs and to influence gene expression (45,46) and alternative splice site decisions (47–49) bound to the N-terminal region containing the predicted zinc finger of FBP21. However, the top hit of the screen represented by the largest number and size of growing yeast clones was the RNA helicase Brr2, which interacted with the C-terminal region of FBP21.

Validation of the interaction between FBP21 and Brr2

As Brr2 plays a key role in the spliceosome, we concentrated on further characterization of the interaction between FBP21 and Brr2. The shortest fragments, for which a Y2H interaction was observed, were the C-terminal region of FBP21 (FBP21$^{200–376}$) and the C-terminal Sec63 unit of Brr2. The interaction between FBP21$^{200–376}$ and Brr2 was validated *in vitro* by size exclusion chromatography (Supplementary Figure S1). Binding was observed with the C-terminal (Brr2^{CC}, residues 1282–2136) but not the N-terminal helicase cassette (Brr2^{NC}, residues 395–1324). The region encompassing both helicase cassettes (Brr2^{HR}, 395–2129) also stably interacted with FBP21$^{200–376}$. The interaction between FBP21$^{200–376}$ and full-length Brr2 (Brr2^{FL}) was weakened by the presence of the Brr2^{NTR}.

To delineate interacting regions of the two proteins, FBP21$^{200–376}$ was chemically cross-linked to Brr2^{CC}, Brr2^{HR} and Brr2^{FL} (constructs shown Figure 1A) and cross-linking sites were identified by mass spectrometry (Figure 1B). The cross-link between FBP21 K338 and Brr2 K1874 was the predominant site with 25, 28 and 21 spectral counts for Brr2^{CC}, Brr2^{HR} and Brr2^{FL}, respectively. This could thus indicate the major interaction site (Figure 1C). Overall, cross-links concentrated on one face of the C-terminal Sec63 unit (Brr2$^{C\text{-}Sec63}$, residues 1840–2136), consistent with data from the Y2H assay, which showed the Sec63 unit as the shortest Brr2 fragment interacting with FBP21. In addition, nearly all cross-links involved the C-terminal 100 residues of FBP21 (FBP21$^{276–376}$).

FBP21$^{276\text{-}376}$ interacts with Brr2$^{C\text{-}Sec63}$ via a complex interface

2D NMR experiments were used to analyze the interaction between Brr2$^{C\text{-}Sec63}$ and FBP21$^{276–376}$ in more detail. First, we isotopically labeled FBP21$^{276–376}$ and recorded a ^{1}H–^{15}N-TROSY-HSQC spectrum with and without Brr2$^{C\text{-}Sec63}$ (Figure 2A). The spectrum of FBP21$^{276–376}$ showed very low chemical shift dispersion, consistent with an intrinsically disordered protein region (IDPR). Upon interaction with Brr2$^{C\text{-}Sec63}$, several resonances exhibited chemical shift changes or line broadening. The spectrum of the complex suggests that the FBP21 fragment globally retains its unstructured nature when bound to Brr2$^{C\text{-}Sec63}$ and does not adopt a stable fold upon complex formation.

Next, we isotopically labeled Brr2$^{C\text{-}Sec63}$ and recorded ^{1}H–^{15}N-TROSY-HSQC spectra with and without

Table 1. Putative interaction partners identified by yeast-two-hybrid for different variants of FBP21

	$FBP21^{FL}$ W191A		$FBP21^{FL}$ W150AW191A + $FBP21^{116-376}$ W150AW191A		$FBP21^{1-50}$		$FBP21^{200-376}$	
	Count	Example	Count	Example	Count	Example	Count	Example
SNRNP200(Brr2)	15		18		-		3	
CYPH (PPIH)	19		19		-		-	
SF3b145 (SF3B2)	20		10		-		-	
SKIP (SNW1)	7		4		-		-	
MORG1 (WDR83)	3		1		-		-	
FAM164A	6		4		-		-	
FAM50B	6		4		-		-	
TIA1	-		-		3		-	
ARGLU1	5		-		3		-	
hnRNPK	4		-		-		-	
ISY1	4		-		-		-	
WBP11	20				-		-	
SF3A1	4		-		-		-	
PRP16 (DHX38)	7		-		-		-	
PRP43 (DHX15)	3		-		-		-	

Fifteen high confidence hits were obtained in the yeast-two-hybrid screen with different constructs of FBP21. The putative interaction partners are organized by the interaction site on FBP21. The count is derived from the number and growth of yeast from each interaction pair.

$FBP21^{276–376}$ (Figure 2B). The interaction resulted in substantial changes of the $Brr2^{C\text{-}Sec63}$ signals, suggesting a large binding interface or conformational changes in $Brr2^{C\text{-}Sec63}$ upon $FBP21^{276–376}$ binding. To better understand this behavior and gain information about the FBP21 binding site on Brr2, we assigned the resonances of the $Brr2^{C\text{-}Sec63}$ spectrum to the backbone-NH-groups. Using conventional triple-resonance spectra in combination with amino acid type-specific labeling (Supplementary Figure S2), we were able to confidently assign the backbone resonances of 78% of the residues of free $Brr2^{C\text{-}Sec63}$ and transfer assignments to $FBP21^{276–376}$-bound $Brr2^{C\text{-}Sec63}$.

Titration of $FBP21^{276–376}$ to $Brr2^{C\text{-}Sec63}$ (Supplementary Figure S3) revealed that most affected resonances showed line broadening at intermediate ligand concentrations, suggesting that the interaction takes place in the intermediate to slow exchange regime relative to the NMR timescale. Mapping the combined $^{1}H–^{15}N$-chemical shift differences of $Brr2^{C\text{-}Sec63}$ upon addition of $FBP21^{276–376}$ (Supplementary Figure S3) onto the crystal structure of $Brr2^{C\text{-}Sec63}$ (PDB ID 4F91; Figure 2C) revealed that the residues with the largest chemical shift differences were located in the HLH domain (residues 1958–2020) and adjacent regions (residues 2043–2055 and 2108–2120). In addition, residues in the HB domain (1857–1915) showed significant chemical shift changes. This suggested an interaction interface on the lower flank of $Brr2^{C\text{-}Sec63}$ (Figure 2C). Some residues located in other areas of $Brr2^{C\text{-}Sec63}$, such as V2066 and V2067 at the interface of the IG-like and the HB domain, also showed chemical shift changes, suggesting that direct interactions between $Brr2^{C\text{-}Sec63}$ and $FBP21^{276–376}$ induce conformational rearrangements of the Sec63 unit. Highly similar chemical shift changes were observed with the shorter $FBP21^{326–376}$ fragment (Supplementary Figure S4), showing that all contacts between FBP21 and $Brr2^{C\text{-}Sec63}$ are formed by the very C-terminal 50 amino acids.

To gain deeper insights into the nature of the interaction, we performed NMR experiments in the presence of a soluble paramagnetic relaxation enhancer (PRE), Gadolinium(III)-diethylenetriaminepentacetate ($Gd(DTPA)^{2-}$, gadopentetic acid) (50), which can lead to signal intensity loss for resonances in a theoretical maximal range of 20–30 Å. (51–53). Since the PRE effect has a dis-

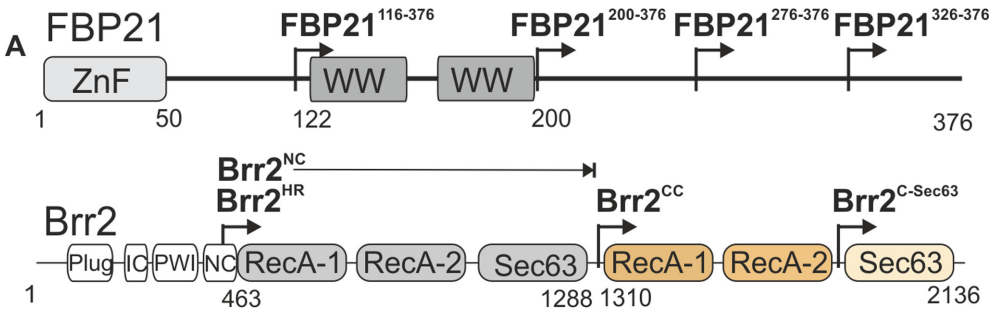

B

FBP21 residue	Brr2 residue: K107	K1567	K1603	K1711	K1841	K1874	K2080	K2087
K250	2							
K270						2		
K274				1		3		
K284		6				3+1		
K286		2			1	1		
K338		5+3+2	2			25+28+21	2	
K365								8+4+1

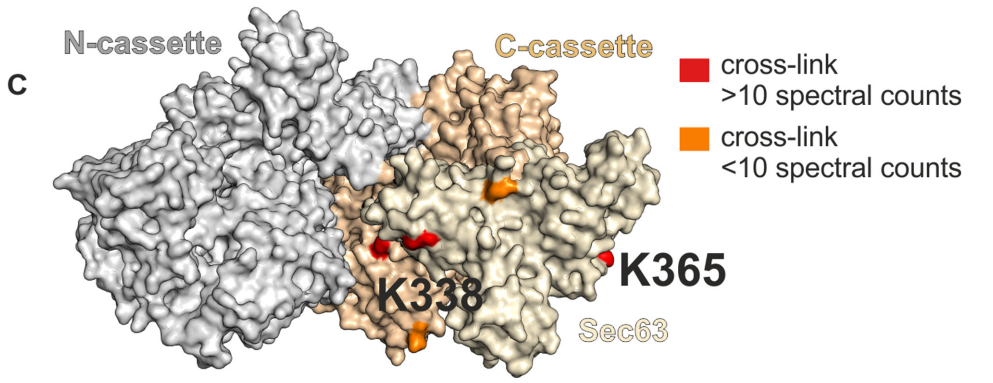

Figure 1. The interaction site between FBP21 and Brr2 as derived from cross-linking. (**A**) Domain organization of FBP21 and Brr2. The domains of the $Brr2^{NTR}$ are shown in white, the domains of $Brr2^{NC}$ in gray, the domains of $Brr2^{CC}$ in light orange. (**B**) Cross-links obtained with $FBP21^{200–376}$ and Brr2 constructs. Numbers in black denote cross-links which were obtained with $Brr2^{CC}$, numbers in blue denote cross-links with $Brr2^{HR}$ and numbers in light blue denote cross-links with $Brr2^{FL}$. (**C**) Cross-linking sites mapped on the structure of Brr2 (PDB ID 4F91). $Brr2^{NC}$ is shown in gray, $Brr2^{CC}$ in light orange and $Brr2^{C\text{-}Sec63}$ in beige. Cross-linked residues with more than 10 spectral counts are colored in red, cross-linked residues with fewer spectral counts in orange.

tance dependency of r^{-6}, strong concentration-dependent loss of signal intensity upon addition of $Gd(DTPA)^{2-}$ was only observed for resonances of surface-exposed residues (Supplementary Figure S5). The experiments were performed with $Brr2^{C\text{-}Sec63}$ alone and in complex with $FBP21^{276–376}$, to qualitatively analyze the interaction interface. Due to strong spectral overlap, a limited number of peaks could be analyzed. Some of these corresponded to residues that were protected by the interaction with $FBP21^{276–376}$, indicating that they are directly involved in binding or that they are changing to a conformation in which they are less surface-exposed. Other residues were deprotected, indicating that the interaction with $FBP21^{276–376}$ resulted in their increased exposure to the PRE. The strongly protected residues clustered around the probable binding site (Figure 2D). Weakly protected and deprotected residues were found mainly at the interface of the IG-like and HB domain. Interestingly, strongly deprotected residues were found at the outward facing end of the IG-like domain. These residues were not affected by $Gd(DTPA)^{2-}$ in free $Brr2^{C\text{-}Sec63}$, probably due to shielding by the negative surface potential of the adjacent HLH domain (Supplementary Figure S8). Interaction with the positively charged $FBP21^{276–376}$ appeared to deprotect this area, making it accessible for PRE.

By using isothermal titration calorimetry (ITC), we determined the dissociation constants of the interaction between $Brr2^{C\text{-}Sec63}$ and various fragments of FBP21 (Figure 3A and Supplementary Figure S6). $FBP21^{200–376}$ interacted with $Brr2^{C\text{-}Sec63}$ in a one-to-one stoichiometry and a K_D of 125 ± 4 nM. The interaction of $FBP21^{276–376}$ with $Brr2^{C\text{-}Sec63}$ displayed a slightly lower affinity with a K_D of

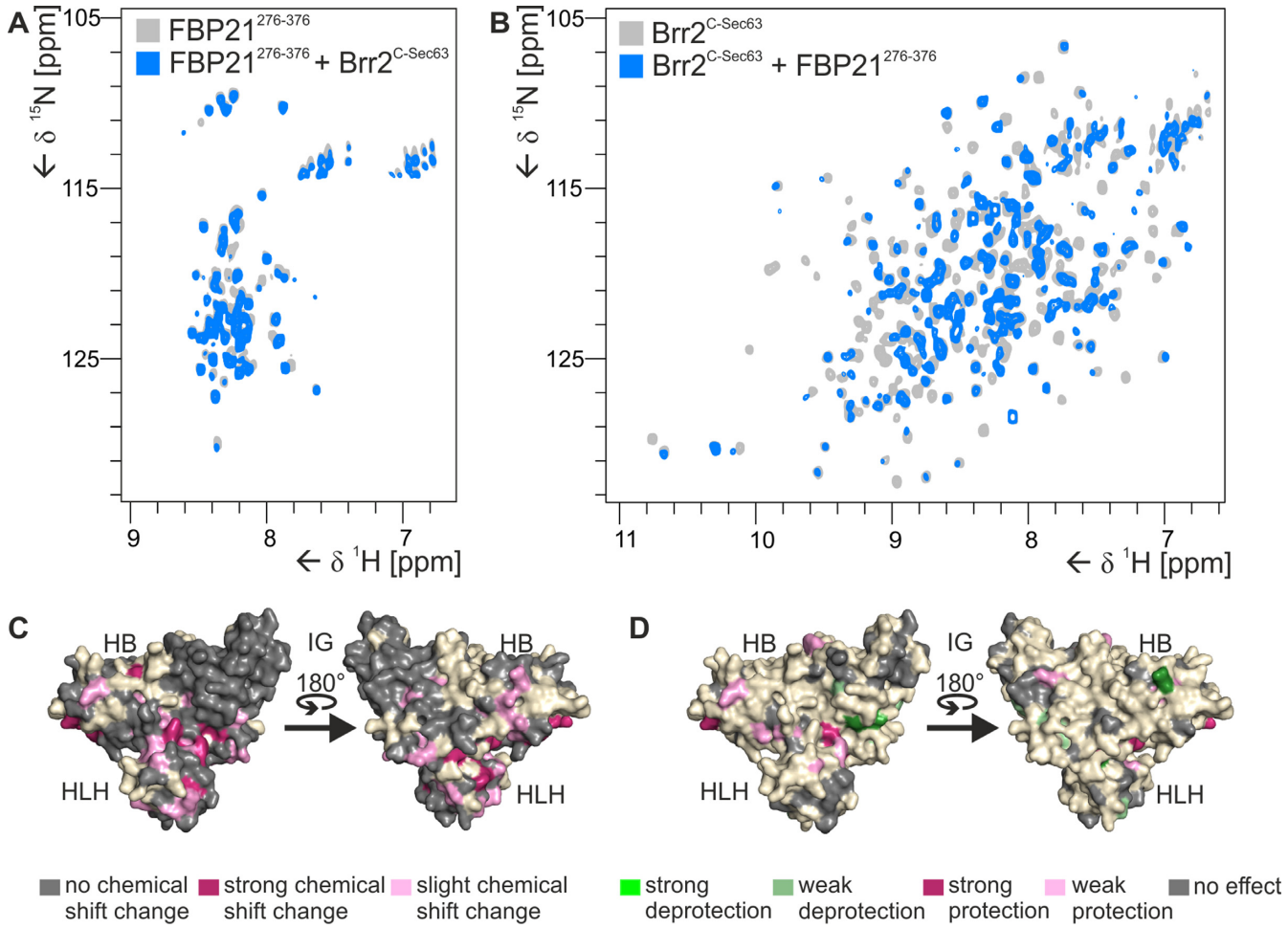

Figure 2. NMR analysis of the interaction between FBP21 and Brr2. (**A**) Overlay of ^{1}H-^{15}N-TROSY-HSQC spectra of 100 μM FBP21$^{276–376}$ alone (gray) and in presence of 200 μM Brr2 $^{C\text{-}Sec63}$ (blue). (**B**) Overlay of ^{1}H-^{15}N-TROSY-HSQC spectra of 100 μM Brr2$^{C\text{-}Sec63}$ alone (gray) and in presence of 200 μM FBP21$^{276–376}$ (blue). (**C**) Assignments and chemical shift changes in presence of 400 μM FBP21$^{276–376}$ mapped on the structure of Brr2$^{C\text{-}Sec63}$ (PDB ID 4F91 (21)) in surface representation. Unassigned residues are shown in beige, assigned residues that have no chemical shift change are shown in dark gray. Residues exhibiting a chemical shift change upon interaction with FBP21$^{276–376}$ are shown in two categories. Dark pink denotes a chemical shift change above the average plus standard deviation of the chemical shift changes of all residues in this experiment ($\Delta\delta = 0.157$ ppm), light pink denotes a chemical shift change above the average chemical shift change of all residues in this experiment ($\Delta\delta = 0.066$ ppm). HB, HLH and IG denote the helical bundle, helix-loop-helix and immunoglobulin-like domain. (**D**) Surface representation of the Sec63 unit with mapped differences in peak intensity loss through Gd(DTPA)$^{2-}$ of free Brr2$^{C\text{-}Sec63}$ and Brr2$^{C\text{-}Sec63}$ in complex with FBP21$^{276–376}$. Residues in beige could not be analyzed due to spectral crowding or missing assignments. Residues in shades of pink were protected by the interaction with FBP21$^{276–376}$, residues in shades of green were more exposed upon interaction.

298 ± 48 nM in a one-to-one stoichiometry. This was unexpected, since cross-linking and NMR analysis indicated that all points of contact are contained in the last 100 residues. The observed difference in binding affinity was due to a higher gain in enthalpy with the longer fragment. The last 50 residues of FBP21, FBP21$^{326–376}$ interacted with a K_D of 110 ± 10 nM. The free enthalpy of the interaction of Brr2$^{C\text{-}Sec63}$ with FBP21$^{276–376}$ and FBP21$^{326–376}$, respectively, was very similar. Both interactions were also entropically favored; however, this effect was stronger for the shorter fragment. These results indicate that an interplay of various enthalpic and entropic effects governs the affinity of the FBP21 fragments towards Brr2$^{C\text{-}Sec63}$.

Interaction between Brr2$^{C\text{-}Sec63}$ and FBP21 is partly mediated by a positively charged stretch in FBP21's C-terminal region

As FBP21$^{200–376}$ is intrinsically disordered and appears to remain disordered upon interaction with Brr2$^{C\text{-}Sec63}$, we reasoned that it would likely utilize peptidic segments for the interaction with Brr2. To delineate such putative epitopes, we performed peptide SPOT analyses (Figure 3B). FBP21 was spotted as overlapping 20mer peptides and binding to various Brr2 constructs was tested (constructs shown in Figure 1A). The SPOT arrays clearly showed that a positively charged stretch in FBP21, ^{357}KKRR^{360}, contained in peptides 56–59, interacts with Brr2^{HR}, Brr2^{CC} and to a lesser extent with Brr2^{FL}. Another positive stretch, ^{116}KKKRK^{122}, contained in peptides 21–24, directly N-

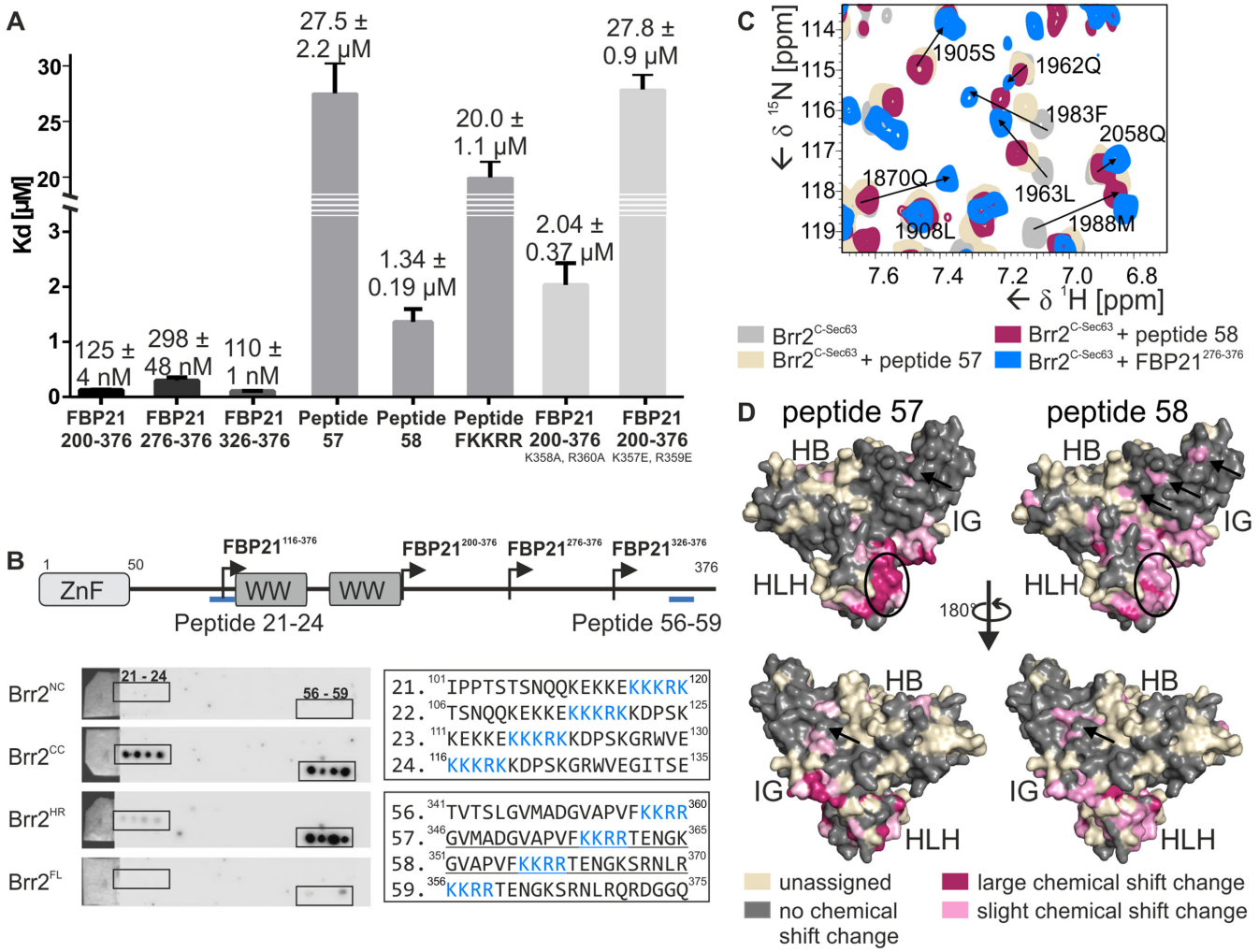

Figure 3. The interaction between FBP21 and Brr2 is partly mediated by a positively charged peptide contained in FBP21's C-terminal region. (**A**) Dissociation constants of FBP21 fragments and Brr2$^{C\text{-}Sec63}$ were determined by ITC. Shown are average K_D values and standard deviations derived from three experiments each. (**B**) Domain organization of FBP21 as in 1A. Blue bars show the location of the peptides interacting with Brr2 derived from the peptide SPOT analysis. Brr2^{CC} and Brr2^{HR} interacted with two regions on the SPOT membrane, both of which contained a positively charged stretch. (**C**) Excerpt of overlaid ^{1}H-^{15}N-TROSY-HSQC spectra of 100 µM Brr2$^{C\text{-}Sec63}$ alone (gray) in presence of sevenfold excess of peptide 57 (beige), in presence of sevenfold excess of peptide 58 (dark pink) and in presence of a 4-fold excess of FBP21$^{276–376}$ (blue). Examples of differentially shifting peaks are shown. (**D**) The binding sites of peptide 57 and peptide 58 was determined by plotting residues with significant chemical shifts changes on the structure of Brr2$^{C\text{-}Sec63}$ (PDB ID 4F91). Unassigned residues are shown in beige, assigned residues that have no or non-significant chemical shift change are shown in dark gray. Residues exhibiting a chemical shift change upon interaction with the peptides are shown in pink as two categories. Dark pink denotes a chemical shift change above the average plus standard deviation of the chemical shift changes of all residues in the experiment ($\Delta\delta = 0.053$ ppm and $\Delta\delta = 0.109$ ppm for peptide 57 and peptide 58, respectively), light pink denotes a chemical shift change above the average chemical shift change of all residues in the experiment ($\Delta\delta = 0.022$ ppm and $\Delta\delta = 0.040$ ppm for peptide 57 and peptide 58, respectively). Circles indicate the negatively charged surface on the HLH domain that is contacted by all measured FBP21 fragments, arrows indicate residues with chemical shift changes outside of the likely binding site. For comparison of the binding sites of peptide 57, peptide 58 and FBP21$^{276–376}$ on Brr2$^{C\text{-}Sec63}$, the residues with chemical shift changes are shown side-by-side using the same thresholds for all experiments in Supplementary Figure S8.

terminal to the WW domains, also mediated an interaction. None of the peptides interacted with Brr2^{NC}.

Peptide 57 (^{346}GVMADGVAPVFKKRRTENGK^{365}, Figure 3B) was synthesized for further analysis. ITC measurements confirmed the interaction between peptide 57 and Brr2$^{C\text{-}Sec63}$. With a K_D of 27.5 ± 2.2 µM, peptide 57 had a substantially lower affinity than the longer fragments FBP21$^{200–376}$ and FBP21$^{276–376}$ (Figure 3A). The interaction took place in a one-to-one stoichiometry and seemed to be predominantly driven by entropy. 2D NMR spectroscopy revealed that the peptide is not sufficient to induce the extensive changes in the spectrum of Brr2$^{C\text{-}Sec63}$ which were observed with FBP21$^{276–376}$ (Figure 3C and Supplementary Figure S7). Fewer resonances showed chemical shift changes upon interaction of Brr2$^{C\text{-}Sec63}$ with peptide 57 and the observed chemical shift differences were substantially smaller. The interaction site was found to be located to a strongly negatively charged area on the HLH domain (indicated by a circle in Figure 3D), which is also part of the binding epitope for FBP21$^{276–376}$. Accordingly,

many glutamate residues were affected by the interaction. M1988, which is flanked by multiple glutamates, showed the largest chemical shift difference. Slight chemical shift changes at the interface between IG-like and HB domain were also observed (indicated by arrows in Figure 3D). However, the HB domain is only affected by FBP21$^{276–376}$ binding, indicating an additional contact.

We also analyzed binding of the core binding motif of peptide 57, ^{356}FKKRR^{360}, to Brr2$^{C\text{-}Sec63}$ by ITC. This peptide showed a similar dissociation constant as peptide 57 (20 ± 1.1 μM), further consolidating an electrostatic interaction. In ITC experiments with two positively charged control peptides, GKKRR and KRFKR, K_D values of 36.95 ± 5.99 μM and 27.29 ± 3.01 μM, respectively, were measured, indicating that a positively charged stretch is mainly responsible for binding to Brr2$^{C\text{-}Sec63}$, while the affinity is slightly increased by the presence of the aromatic phenylalanine (Supplementary Figure S6).

To further test if and to which extent the positively charged stretch of FBP21, ^{356}FKKRR^{360}, contributes to the interaction with Brr2$^{C\text{-}Sec63}$ in context of longer FBP21 fragments, we mutated pairs of positively charged residues in this region of FBP21$^{200–376}$ to alanine (K358A/R360A) or glutamate (K357E/R359E). ITC experiments showed that both mutants still interacted with Brr2$^{C\text{-}Sec63}$, albeit with a reduced affinity in comparison to the wild type (K_D of 2.04 ± 0.37 μM and 27.8 ± 0.9 μM for FBP21$^{200–376}$ K358A/R360A and FBP21$^{200–376}$ K357E/R359E, respectively). The ^{1}H–^{15}N-TROSY-HSQC spectrum of Brr2$^{C\text{-}Sec63}$ displayed similar chemical shift changes upon the addition of the glutamate mutant of FBP21$^{200–376}$ as upon addition of the wild-type FBP21$^{276–376}$ variant (Supplementary Figure S4). The positively charged stretch thus aids FBP21 to bind Brr2$^{C\text{-}Sec63}$ but is not responsible for the strong changes in the NMR spectrum, which seem to additionally require secondary binding sites.

We wondered whether these binding sites would be found in proximity to the positively charged sequence and thus also analyzed the interaction of Brr2$^{C\text{-}Sec63}$ with peptide 58 (^{351}GVAPVFKKRRTENGKSRNLR^{370}). ITC measurements revealed a much lower K_D value of 1.34 ± 0.19 μM and a large enthalpic contribution to the interaction. This was surprising, since peptide 57 and peptide 58 overlap to 75%. NMR experiments (Figure 3C and Supplementary Figure S7) revealed that binding of peptide 58 to Brr2$^{C\text{-}Sec63}$ induced chemical shift changes that were intermediate between peptide 57 and FBP21$^{276–376}$ in number and magnitude. Figure 3C shows the differential effects of binding by peptide 57, peptide 58 and FBP21$^{276–376}$ on the chemical shifts of Brr2$^{C\text{-}Sec63}$ in a representative part of the ^{1}H–^{15}N-TROSY-HSQC spectrum. Some resonances are affected by all ligands in a similar fashion (e.g. 1988M) or show chemical shift changes with increasing magnitudes upon interaction with peptide 57, peptide 58 and FBP21$^{276–376}$ (e.g. 1983F and 1963L). Still, several peaks only showed significant chemical shift changes upon the interaction with FBP21$^{276–376}$ (e.g. 1905S, 1870Q and 2058Q). Mapping of chemical shift changes on the structure of Brr2$^{C\text{-}Sec63}$ revealed a larger binding epitope for peptide 58 than for peptide 57 (Figure 3D and Supplementary Figure S8), encompassing the negatively charged HLH domain that was also contacted by peptide 57 (indicated by a circle in Figure 3D) and the interface of the HLH, HB and IG-like domains. In addition, strong chemical shift changes of residues at the interface of HB and IG domains were observed (indicated by arrows in Figure 3D). However, the lower flank of the HB domain was not contacted by peptide 58, indicating that an additional sequence of FBP21 binds to this area, also contributing to an additional tenfold affinity increase (K_D = 110 ± 10 nM for the interaction between FBP21$^{326–376}$ and Brr2$^{C\text{-}Sec63}$).

Binding of FBP21$^{200\text{-}376}$ to Brr2^{HR} leads to reduction of the Brr2 unwinding activity

To investigate potential functional consequences of the interaction between FBP21$^{200–376}$ and Brr2, we analyzed the influence of the interaction on the RNA helicase activity of Brr2 *in vitro*. Unwinding of the U4/U6 di-snRNA by various Brr2 constructs was analyzed in absence and presence of 600 nM FBP21$^{200–376}$, which equals a six-fold excess over Brr2 (Figure 4A). The unwinding activity of Brr2^{NC} was unchanged upon addition of FBP21$^{200–376}$ (Figure 4A), consistent with the FBP21 fragment contacting only the C-terminal cassette. In contrast, the apparent unwinding rate of Brr2^{HR} was reduced nearly by half, to a level that was closer to the unwinding rate of the isolated Brr2^{NC}. Brr2^{FL} was only slightly inhibited by FBP21$^{200–376}$. This observation is in line with the observed lower affinity of Brr2^{FL} to FBP21$^{200–376}$ (Supplementary Figure S1). When using higher concentrations of FBP21$^{200–376}$ in the unwinding assay with Brr2^{HR} (1–10 μM), the unwinding rate was further reduced, but more noticeably, the unwound fraction was strongly decreased (Figure 4D and Supplementary Figure S10), indicating a pool of U4/U6 di-snRNA which cannot be unwound by Brr2. These results suggest that FBP21$^{200–376}$ can inhibit Brr2 helicase activity by two distinct mechanisms. At low concentrations, the fragment may predominantly bind the Brr2 C-terminal cassette and functionally uncouple the two cassettes of Brr2, leading to reduction of the unwinding rate. At high concentrations, FBP21$^{200–376}$ may additionally bind the U4/U6 di-snRNA and make it unavailable for unwinding by Brr2, leading to the observed lower amplitude of unwinding.

To test the above hypotheses, we conducted RNA binding studies with FBP21$^{200–376}$. At concentrations above 400 nM, FBP21$^{200–376}$ induced electrophoretic mobility shifts of U4/U6 di-snRNA (Supplementary Figure S9). Quantification of the data revealed an apparent K_D of 0.78 μM for the interaction. The affinity for U4 snRNA was significantly lower (apparent K_D = 3.5 μM, Figure 4B), and no interaction could be detected with U6 snRNA (data not shown). FBP21$^{200–376}$ at a concentration of 5 μM, which equals a 60-fold excess at the final point of the titration, competed with Brr2 for RNA binding and reduced the affinity between U4/U6 duplex and Brr2^{HR} by a factor of five (Figure 4C). In contrast, at low concentrations (600 nM), FBP21$^{200–376}$ had little effect on RNA binding by Brr2^{HR} (Figure 4C), indicating that the observed lower unwinding amplitude is not caused by direct substrate competition.

To further test the influence of RNA binding by FBP21 on U4/U6 di-snRNA unwinding by Brr2, we performed

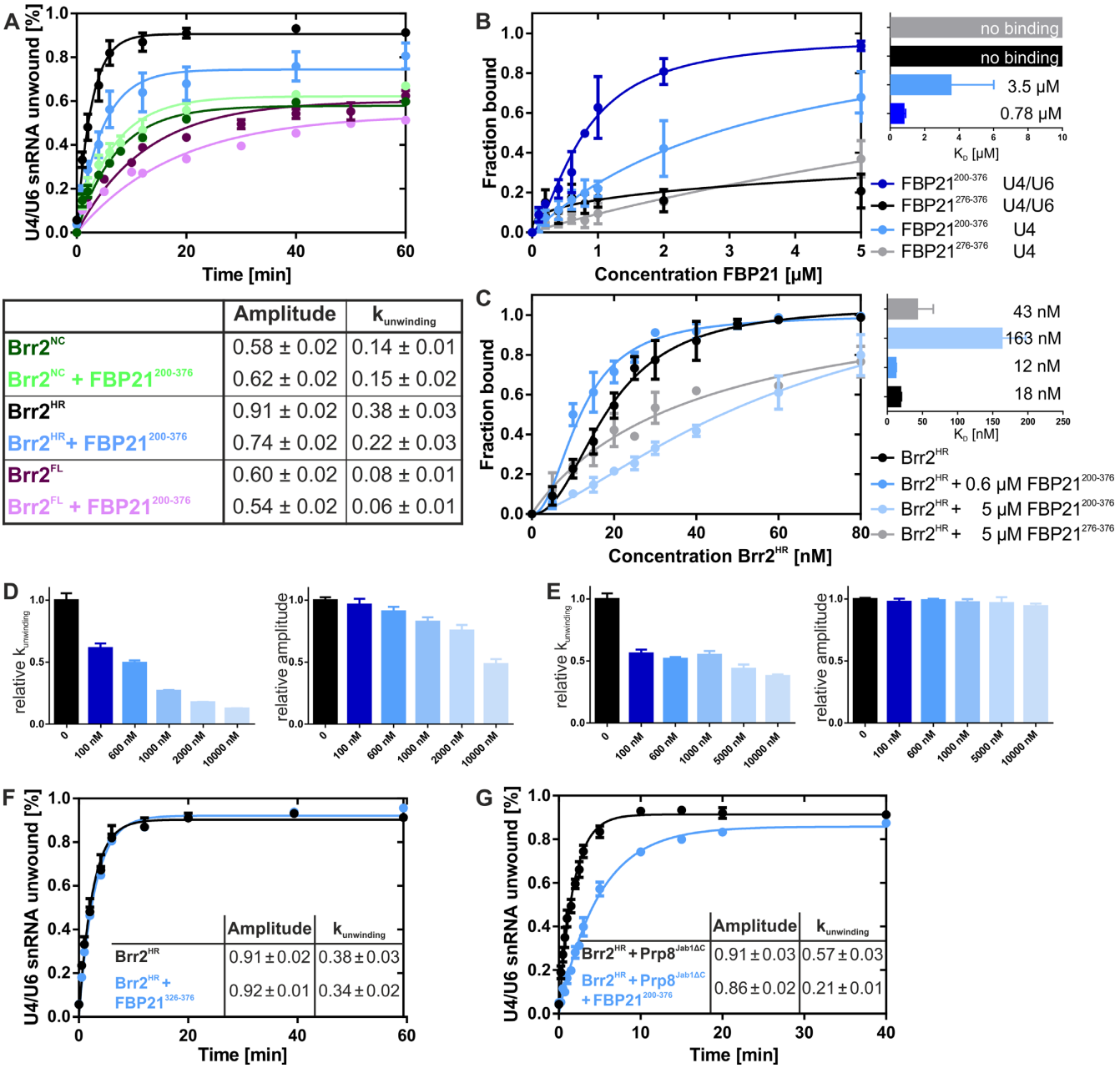

	Amplitude	$k_{unwinding}$
Brr2^{NC}	0.58 ± 0.02	0.14 ± 0.01
Brr2^{NC} + FBP21$^{200-376}$	0.62 ± 0.02	0.15 ± 0.02
Brr2^{HR}	0.91 ± 0.02	0.38 ± 0.03
Brr2^{HR}+ FBP21$^{200-376}$	0.74 ± 0.02	0.22 ± 0.03
Brr2^{FL}	0.60 ± 0.02	0.08 ± 0.01
Brr2^{FL} + FBP21$^{200-376}$	0.54 ± 0.02	0.06 ± 0.01

	Amplitude	$k_{unwinding}$
Brr2^{HR}	0.91 ± 0.02	0.38 ± 0.03
Brr2^{HR} + FBP21$^{326-376}$	0.92 ± 0.01	0.34 ± 0.02

	Amplitude	$k_{unwinding}$
Brr2^{HR} + Prp8$^{Jab1\Delta C}$	0.91 ± 0.03	0.57 ± 0.03
Brr2^{HR} + Prp8$^{Jab1\Delta C}$ + FBP21$^{200-376}$	0.86 ± 0.02	0.21 ± 0.01

Figure 4. FBP21 regulates the helicase activity of Brr2 by two distinct mechanisms. (**A**) U4/U6 di-snRNA unwinding assays with 100 nM Brr2^{NC}, Brr2^{HR} and Brr2^{FL} and absence and presence of 600 nM FBP21$^{200–376}$. Unwinding rate ($k_{unwinding}$) and amplitudes are given in the table. FBP21$^{200–376}$ strongly inhibits Brr2^{HR} and slightly inhibits Brr2^{FL}. (**B**) U4/U6 di-snRNA and U4 snRNA binding of FBP21 fragments derived from EMSA experiments and affinites derived from fitting. (**C**) U4/U6 snRNA binding of Brr2^{HR} derived from EMSA experiments in presence of FBP21$^{200–376}$ or FBP21$^{276–376}$. FBP21$^{200–376}$ inhibits RNA binding of Brr2^{HR} when present in high concentrations. The inhibition is reduced when the shorter FBP21$^{276–376}$ is used in the assay. (**D**) Concentration dependence of the inhibition of Brr2^{HR} by FBP21$^{200–376}$. The relative unwinding rate and relative reaction amplitude decrease with increasing concentrations of FBP21. (**E**) Concentration dependence of the inhibition of Brr2^{HR} by FBP21$^{276–376}$. The unwinding rate is reduced in a concentration-independent manner when a stoichiometric complex is formed. The relative amplitude stays constant at all concentrations. (**F**) U4/U6 di-snRNA unwinding assays with 1 μM FBP21$^{326–376}$ show that FBP21$^{326–376}$ has no inhibitory effect on Brr^{HR}. (**G**) U4/U6 di-snRNA unwinding assays of 100 μM Brr2^{HR} in presence of equimolar amounts of Prp8$^{Jab1\Delta C}$ with or without 600 nM FBP21$^{200–376}$. The activatory effect of Prp8$^{Jab1\Delta C}$ is completely abolished in presence of FBP21$^{200–376}$. All datapoints were taken in at least three independent replicates. The plots show the average and standard deviation of the collected datapoints. Unwinding rates and amplitudes are given as best-fit values ± standard error.

unwinding assays with FBP21$^{276–376}$ (Figure 4E and Supplementary Figure S10) which did not interact with U4/U6 di-snRNA in electrophoretic mobility shift assay (EMSAs) (Figure 4B and Supplementary Figure S9). As expected, FBP21$^{276–376}$ reduced the unwinding rate of Brr2^{HR} approximately two-fold, similar to FBP21$^{200–376}$. However, experiments employing high concentrations of FBP21$^{276–376}$ revealed the same reduction in unwinding rate, but no decrease in the unwound fraction (Figure 4E and Supplementary Figure S9). We thus conclude that the interaction of FBP21 with Brr2^{HR} directly modulates helicase activity by functionally uncoupling N- and C-terminal cassettes, and that FBP21 at higher concentrations additionally inhibits the unwinding of a pool of U4/U6 di-snRNA by a yet unknown mechanism that depends on the direct interaction of FBP21 with the U4/U6 di-snRNA.

Interestingly, the shorter FBP21$^{326–376}$ did not affect Brr2^{HR} helicase activity. This indicates that although FBP21$^{326–376}$ covers the complete binding site on Brr2$^{C\text{-}Sec63}$, it lacks additional contacts that appear to be responsible for helicase inhibition and may also increase the interaction affinity (Figure 4F). Cross-links at the interface of Brr2$^{C\text{-}Sec63}$ and the C-terminal RecA-2 domain to FBP21$^{200–376}$ suggest that the contacts are made in this area.

Interplay with other spliceosomal components

Brr2 is known to be regulated by the C-terminal Jab1 domain of Prp8. The intrinsically disordered tail can intermittently inhibit Brr2, while a C-terminally truncated version of the Jab1 domain (Prp8$^{Jab1\Delta C}$) acts as a strong activator of the Brr2 helicase. We thus asked whether the inhibitory effect of FBP21 is still observed when Brr2 is bound to Prp8$^{Jab1\Delta C}$. Size exclusion chromatography revealed that FBP21$^{276–376}$ can bind simultaneously with Prp8$^{Jab1\Delta C}$ to Brr2^{HR} (Supplementary Figure S1). Interestingly, this was not the case for FBP21$^{326–376}$. Unwinding assays showed that the Prp8$^{Jab1\Delta C}$ activation of Brr2^{HR} helicase activity is strongly reduced in the presence of FBP21$^{200–376}$ (from 0.57 min^{-1} to 0.21 min^{-1}; Figure 4G). In summary, it appears that Prp8$^{Jab1\Delta C}$ and FBP21 compete for Brr2^{HR} regulation, which may be important for timing of FBP21-mediated inhibition and Prp8$^{Jab1\Delta C}$-mediated activation.

FBP21 is known to interact with PRS via its WW domains. As the PRS in the C-terminal tail of SmB/B' is a well-described interaction partner of FBP21 (37,54), we wondered whether the interactions between FBP21 and Brr2 and FBP21 and the SmB-derived peptide (GTPMGM PPPGMRPPPPGMRGLL) are independent of each other. ITC experiments were performed with a fragment of FBP21 that encompasses the WW domains and the Brr2-binding C-terminal domain (FBP21$^{116–376}$) (Supplementary Figure S11). The direct interaction between each set of interaction partners was analyzed. The dissociation constant between FBP21$^{116–376}$ and SmB-peptide was found to be 16.8 ± 3.0 μM, which is in agreement with previously reported K_D values (37). The dissociation constant between FBP21$^{116–376}$ and Brr2$^{C\text{-}Sec63}$ was 275 ± 106 nM, which agrees with the K_D values that were measured for the other fragments (Supplementary Figure S6). Brr2$^{C\text{-}Sec63}$ itself did not interact with the SmB-peptide (Supplementary Figure S11). The interactions of FBP21$^{116–376}$ with SmB-peptide and FBP21$^{116–376}$ with Brr2$^{C\text{-}Sec63}$ after pre-incubation of FBP21$^{116–376}$ with the respective other binding partner showed K_D values of 14.0 ± 0.8 μM and 194 ± 14 nM, respectively. This is in good agreement with the dissociation constants of the binary interactions and shows that they occur independently (Supplementary Figure S11). *In vitro* unwinding assays showed that FBP21$^{116–376}$ inhibited the Brr2^{HR} helicase activity to a similar extent as FBP21$^{200–376}$ (Supplementary Figure S11H). Together, these results suggest that the inhibitory effect of FBP21 on Brr2 and the interactions of FBP21 with SmB are orthogonal and allow the construction of a model, in which FBP21 interacts with both proteins in the context of the B complex (Figure 5).

DISCUSSION

Here, we have used a yeast-two-hybrid screen in combination with biochemical and biophysical analyses to uncover a molecular function of the B complex-specific protein FBP21. We identified 15 putative spliceosomal FBP21 interaction partners. Many of them are consistent with a role in the B complex; among them are core spliceosomal proteins (Brr2, SF3B2, SF3A1) (31), the U4/U6-related protein PPIH (31,55) and some putative interaction partners that are implicated mainly in splice site definition (ARGLU1, TIA-1, hnRNPK) and may also be present in later stages (56). A couple of the identified interaction partners are predominantly found in later stages, such as the Prp19-associated ISY1 (57) and WBP11 (31,58), the B^{act} complex associated SKIP (59), the C complex-associated MORG1 (31) and the helicases Prp16 and Prp43. ISY1, WBP11 and SKIP are also found to a minor extent in the B complex (31), allowing for an interaction at this stage. Many of the interactions with later stage proteins (WBP11, ISY1, Prp16 and Prp43) are PRS-mediated and may therefore be detected independent of the spliceosomal complex they are associated with.

The interaction with the spliceosomal RNA helicase Brr2 was analyzed in further detail. We found that FBP21 interacts via its C-terminal region (residues 200–376) with the C-terminal cassette of Brr2. The interaction is mediated to a large extend by the C-terminal Sec63 unit of Brr2 and depends on a network of multiple contacts.

A positively charged stretch in FBP21 (residues 356–360) confers interaction affinity and may play a role for establishing a primary contact between the proteins. The interaction takes place at the HLH domain of the C-terminal Sec63 unit in Brr2 (residues 1960–2020), and its interface to the HB and IG domains (binding site A in Figure 5) as revealed by NMR measurements. The cross-linking data confirmed that the very C-terminal region of FBP21 containing the positively charged stretch is oriented towards the IG and HLH domains of the Brr2 C-terminal cassette. This area presents a strongly negatively charged surface due to an accumulation of glutamate residues. This feature is not seen in the N-terminal Sec63 unit, explaining why despite its highly similar structure, the N-terminal Sec63 unit does not interact with FBP21. The interaction is strongly favored by an entropy gain, which is common for electrostatic interactions.

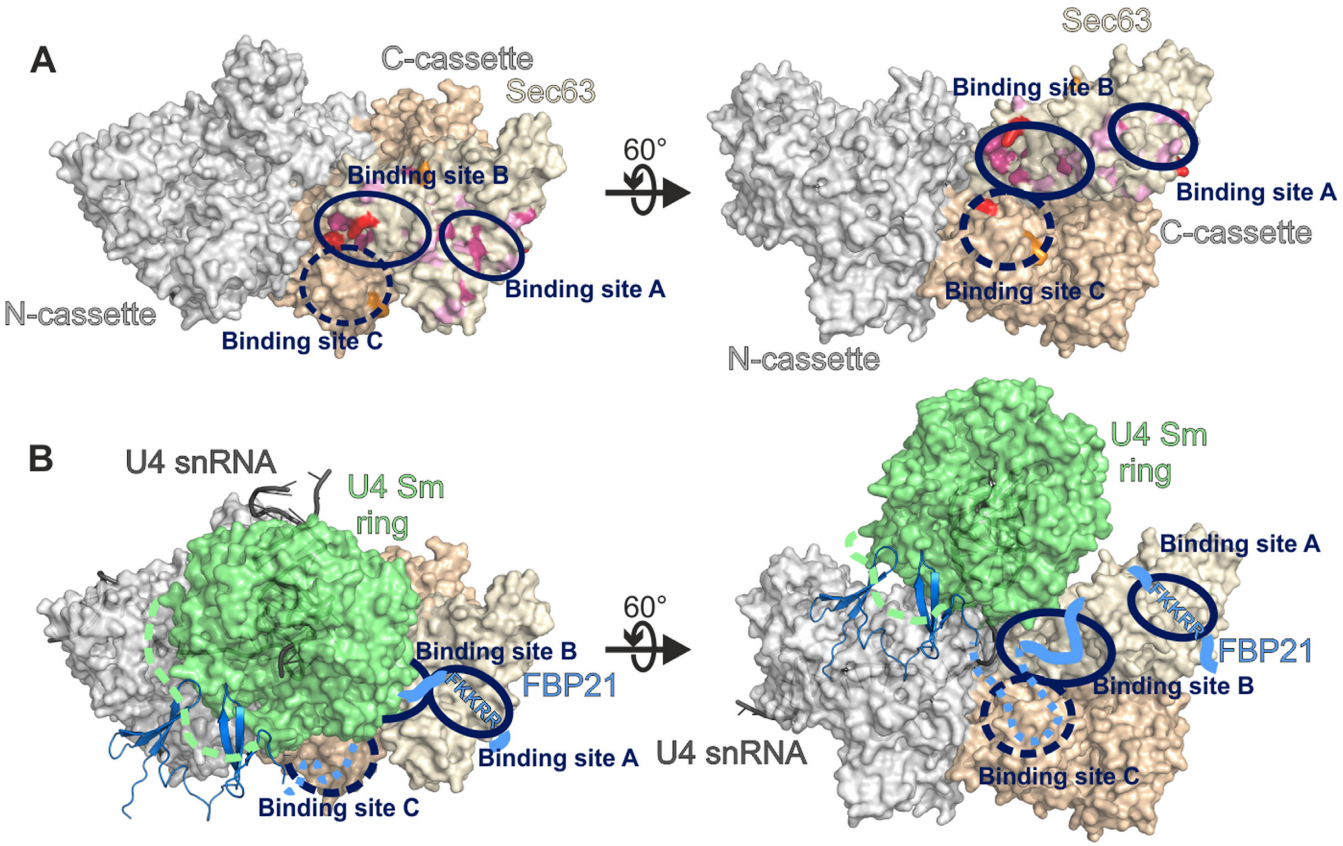

Figure 5. A model of FBP21 in the spliceosome. (**A**) Binding site of FBP21 on Brr2. The N-terminal helicase cassette is shown in gray, the C-terminal helicase cassette in light orange and the C-terminal Sec63 domain in beige. Pink and light pink residues showed chemical shift changes in NMR experiments with FBP21$^{276–376}$. Residues that cross-linked to FBP21$^{200–376}$ are shown in red (>10 spectral counts) and orange (<10 spectral counts). From these experiments, three contact sites were derived. (**B**) FBP21 interacts with Brr2 via the binding sites described in A. FBP21 is drawn in blue. Areas in which the interaction site is well established are drawn with a solid line, areas about which less information is available are drawn in dashed lines. FBP21 additionally interacts with SmB/B' (Sm ring in green, C-terminal tail of SmB/B' shown as a green dashed line) via its WW domains (PDB ID 2JXW). The orientation of Brr2, and the structure of the Sm ring and the U4 RNA are derived from an 'activated' yeast U4/U6•U5 tri-snRNP (PDB ID 5GAN).

The region directly C-terminal to the positively charged stretch in FBP21 also contacts the Sec63 unit, leading to more pronounced chemical shift changes and an increased binding affinity for a peptide comprising both elements. Interestingly, this contact induced stronger chemical shift changes between the HB and IG domains, distant from the probable binding site (Figure 3D and Supplementary Figure S8). These chemical shift changes likely arise from a minor conformational rearrangement rather than from a direct interaction. This is supported by the finding that binding of FBP21$^{276–376}$ to the Sec63 unit leads to a change in surface exposure of residues in that area (Figure 2D).

An additional contact is established between the C-terminal region of FBP21 and the C-terminal Sec63 unit of Brr2, which leads to higher affinity through a strong enthalpy gain upon complex formation. We observed strong chemical shift changes in the NMR spectrum of Brr2$^{C\text{-}Sec63}$ upon addition of FBP21$^{276–376}$, which affects residues that are localized mainly on an extended surface epitope, which stretches across the Sec63 unit towards the RecA-2 domain of Brr2^{CC} (binding site B in Figure 5). This binding interface agrees both with strongly protected areas in the PRE experiments and with the observed cross-links.

The region of FBP21 (within residues 326–356), which occupies binding site B on Brr2$^{C\text{-}Sec63}$, was not identified in the peptide SPOT array. One explanation for this observation could be that the additional contact site requires the formation of a secondary structure in FBP21, which is not adopted by the isolated peptide. While we cannot exclude more transiently formed secondary structures to be populated in the bound state, the HSQC spectrum of FBP21$^{276–376}$ appeared to remain consistent with an IDPR upon binding. Another possible explanation is that FBP21 remains largely unstructured upon binding to Brr2 and forms a so-called fuzzy complex, i.e. a complex which samples various bound conformations (60). This type of interaction would be difficult to replicate with a short peptide and would thus not show up in a SPOT array. A fuzzy FBP21–Brr2 interaction would also explain our difficulties to crystallize the complex and may rationalize the different enthalpic and entropic properties of the interaction made by different FBP21 fragments.

Using its C-terminal 100 residues, FBP21 also contacts regions of Brr2^{CC} outside of the Sec63 unit (binding site C in Figure 5), as indicated by the differential effects of FBP21 fragments with different lengths on the Brr2 helicase ac-

tivity. These extended interactions are important for direct FBP21-dependent Brr2 modulation.

The interaction of FBP21 with Brr2 influences Brr2 helicase activity *in vitro* by two distinct mechanisms. FBP21 reduces the pool of U4/U6 di-snRNA that can be unwound by Brr2 by interacting itself with the U4/U6 di-snRNA. Since only a large excess of FBP21 reduces the apparent affinity of Brr2 for its substrate, this is likely not a consequence of direct competition. However, blocking of the Brr2 binding site may be possible at particular stages of splicing, e.g. during pre-B to B complex transition when all factors are present at high effective concentrations in the spliceosome, but Brr2 is not yet bound to its substrate. Possibly, FBP21 could also interact with Brr2 and the U4/U6 di-snRNA simultaneously, which may lead to stalling of the helicase and thereby to the observed lower unwinding amplitude. Future investigations will hopefully further elucidate the mechanism by which RNA-binding of FBP21 influences the unwinding reaction.

Moreover, our observation that the interaction of $FBP21^{276–376}$ with $Brr2^{CC}$ leads to a decrease of the apparent unwinding rate of $Brr2^{HR}$ indicates that FBP21 additionally influences one or several steps of Brr2-mediated U4/U6 unwinding directly. In isolated Brr2, the inactive C-terminal cassette acts as an intramolecular cofactor that stimulates the helicase activity of the N-terminal cassette by direct or indirect (e.g. via the substrate) interactions between the cassettes. Based on our observations, we suggest that FBP21 binding to the C-terminal cassette allosterically modulates the intramolecular contacts and thus the functional communication between the Brr2 helicase cassettes. Consistent with this interpretation, addition of FBP21 to $Brr2^{HR}$ reduces the unwinding activity to the level of the isolated N-terminal cassette.

The functional interplay between FBP21, $Brr2^{HR}$ and $Prp8^{Jab1\Delta C}$ may also be governed by allostery. FBP21 and $Prp8^{Jab1\Delta C}$ do not compete for an interaction site on $Brr2^{HR}$, however, while $FBP21^{276–376}$ forms a stable complex with $Brr2^{HR}$-$Prp8^{Jab1\Delta C}$, $FBP21^{326–376}$ is not able to stably associate with a pre-formed $Brr2^{HR}$–$Prp8^{Jab1\Delta C}$ complex. Thus, the additional contact of the longer FBP21 fragment, which also influences helicase activity, is necessary for the protein to bind Brr2 in presence of $Prp8^{Jab1\Delta C}$. Meanwhile, FBP21 binding overrides the helicase activating effect of $Prp8^{Jab1\Delta C}$ in unwinding assays. Therefore, FBP21 and $Prp8^{Jab1\Delta C}$ seem to compete for Brr2 regulation—$Prp8^{Jab1\Delta C}$ may induce an 'activated' conformation, which is incompatible with binding of the truncated FBP21 fragment. In contrast, FBP21 binding may induces a 'muted' conformation, which allows for $Prp8^{Jab1\Delta C}$ binding but inhibits the activation by $Prp8^{Jab1\Delta C}$.

Other splicing factors have been shown to interact with the C-terminal cassette of Brr2 (27,28,30,61) although the exact binding sites are unknown for most of them. It will be highly interesting to see whether these proteins also exert an effect on Brr2 helicase activity and regulate the helicase in the different spliceosomal complexes.

The interaction between FBP21 and Brr2 we described in this study is very likely to have important effects during splicing. FBP21 is thought to be stably integrated into the spliceosome exclusively at the B complex stage (31). Although no structure of a human spliceosomal B complex is yet available, recent structural studies of U4/U6•U5 tri-snRNPs provide some insight into how FBP21-dependent Brr2 regulation could take place. The position of Brr2 is drastically different in structures of human and yeast U4/U6•U5 tri-snRNPs (30,62,63). In the human tri-snRNP structure, Brr2 is located remote from its U4/U6 substrate and its N-terminal region is wrapped around the helicase core. In this 'resting' conformation, the tri-snRNP is stable in the presence of ATP. Since the interaction of FBP21 with Brr2 in the locked conformation is considerably weakened, this situation can explain why FBP21 does not stably associate with the tri-snRNP via Brr2 outside of the spliceosome. In stark contrast, in the yeast tri-snRNP structure, Brr2 is bound to its U4/U6 substrate and seems poised for unwinding, consistent with the observed lability of this particle in the presence of ATP (30). The $Brr2^{NTR}$ is peeled off the helicase region and is engaged in protein-protein interactions with other subunits of the tri-snRNP. The yeast tri-snRNP structure could thus resemble the state of the tri-snRNP within the B complex immediately before Brr2-mediated U4/U6 unwinding is initiated. Within this structure, $Brr2^{CC}$ and in particular $Brr2^{C\text{-}Sec63}$ are exposed and could easily engage in an interaction with FBP21. The Sm ring of U4 is located in close proximity. FBP21 might thus employ its WW domains to additionally interact with the PRS-tail of SmB. This would likely reinforce the direct effect FBP21 can exert on Brr2, thus delaying U4/U6 unwinding and thereby spliceosome activation.

In conclusion, we have identified a novel role for FBP21 as a key player in Brr2 regulation. FBP21 modulates the two helicase cassettes of Brr2 and affects snRNA binding and unwinding at a checkpoint of splicing regulation. As FBP21 was suggested previously to modulate alternative splicing, it will be interesting to see how FBP21-mediated Brr2 inhibition translates into distinct splice site decision in the cell.

DATA ACCESS

Backbone assignments of $Brr2^{C\text{-}Sec63}$ were deposited at the BMRB (Accession number 27135).

SUPPLEMENTARY DATA

Supplementary Data are available at NAR Online.

ACKNOWLEDGEMENTS

We would like to thank Eliot Morrison for providing a script with which chemical shift predictions and resonances from selectively labeled proteins could be matched efficiently.

FUNDING

Collaborative Research Center SFB765 [project C4] and SFB958 [project A07 to C.F.]; Collaborative Research Center SFB740 [Project A04 to M.C.W.]; Einstein Stiftung Berlin [Project A-2012-140 to M.C.W.]; Dahlem International Network PostDoc grant from Freie Universität Berlin (to K.F.S.).

Conflict of interest statement. None declared.

REFERENCES

1. Wahl,M.C., Will,C.L. and Luhrmann,R. (2009) The spliceosome: design principles of a dynamic RNP machine. *Cell*, **136**, 701–718.
2. Fabrizio,P., Dannenberg,J., Dube,P., Kastner,B., Stark,H., Urlaub,H. and Luhrmann,R. (2009) The evolutionarily conserved core design of the catalytic activation step of the yeast spliceosome. *Mol. Cell*, **36**, 593–608.
3. Lopez,P.J. and Seraphin,B. (1999) Genomic-scale quantitative analysis of yeast pre-mRNA splicing: implications for splice-site recognition. *RNA*, **5**, 1135–1137.
4. Barrass,J.D. and Beggs,J.D. (2003) Splicing goes global. *Trends Genet.*, **19**, 295–298.
5. Sakharkar,M.K., Chow,V.T. and Kangueane,P. (2004) Distributions of exons and introns in the human genome. *In Silico Biol.*, **4**, 387–393.
6. Lander,E.S., Linton,L.M., Birren,B., Nusbaum,C., Zody,M.C., Baldwin,J., Devon,K., Dewar,K., Doyle,M., FitzHugh,W. *et al.* (2001) Initial sequencing and analysis of the human genome. *Nature*, **409**, 860–921.
7. Ast,G. (2004) How did alternative splicing evolve? *Nat. Rev. Genet.*, **5**, 773–782.
8. Black,D.L. (2003) Mechanisms of alternative pre-messenger RNA splicing. *Annu. Rev. Biochem.*, **72**, 291–336.
9. Xiong,H.Y., Alipanahi,B., Lee,L.J., Bretschneider,H., Merico,D., Yuen,R.K., Hua,Y., Gueroussov,S., Najafabadi,H.S., Hughes,T.R. *et al.* (2015) RNA splicing. The human splicing code reveals new insights into the genetic determinants of disease. *Science*, **347**, 1254806.
10. Cieply,B. and Carstens,R.P. (2015) Functional roles of alternative splicing factors in human disease. *Wiley Interdiscip. Rev. RNA*, **6**, 311–326.
11. Cooper,T.A., Wan,L. and Dreyfuss,G. (2009) RNA and disease. *Cell*, **136**, 777–793.
12. Oltean,S. and Bates,D.O. (2014) Hallmarks of alternative splicing in cancer. *Oncogene*, **33**, 5311–5318.
13. Hoskins,A.A., Rodgers,M.L., Friedman,L.J., Gelles,J. and Moore,M.J. (2016) Single molecule analysis reveals reversible and irreversible steps during spliceosome activation. *Elife*, **5**, e14166.
14. Laggerbauer,B., Achsel,T. and Luhrmann,R. (1998) The human U5-200kD DEXH-box protein unwinds U4/U6 RNA duplices in vitro. *Proc. Natl. Acad. Sci. U.S.A.*, **95**, 4188–4192.
15. Raghunathan,P.L. and Guthrie,C. (1998) RNA unwinding in U4/U6 snRNPs requires ATP hydrolysis and the DEIH-box splicing factor Brr2. *Curr. Biol.*, **8**, 847–855.
16. Lauber,J., Fabrizio,P., Teigelkamp,S., Lane,W.S., Hartmann,E. and Luhrmann,R. (1996) The HeLa 200 kDa U5 snRNP-specific protein and its homologue in Saccharomyces cerevisiae are members of the DEXH-box protein family of putative RNA helicases. *EMBO J.*, **15**, 4001–4015.
17. Noble,S.M. and Guthrie,C. (1996) Identification of novel genes required for yeast pre-mRNA splicing by means of cold-sensitive mutations. *Genetics*, **143**, 67–80.
18. Bessonov,S., Anokhina,M., Will,C.L., Urlaub,H. and Luhrmann,R. (2008) Isolation of an active step I spliceosome and composition of its RNP core. *Nature*, **452**, 846–850.
19. Absmeier,E., Santos,K.F. and Wahl,M.C. (2016) Functions and regulation of the Brr2 RNA helicase during splicing. *Cell Cycle*, **15**, 3362–3377.
20. Absmeier,E., Wollenhaupt,J., Mozaffari-Jovin,S., Becke,C., Lee,C.T., Preussner,M., Heyd,F., Urlaub,H., Luhrmann,R., Santos,K.F. *et al.* (2015) The large N-terminal region of the Brr2 RNA helicase guides productive spliceosome activation. *Genes Dev.*, **29**, 2576–2587.
21. Santos,K.F., Jovin,S.M., Weber,G., Pena,V., Luhrmann,R. and Wahl,M.C. (2012) Structural basis for functional cooperation between tandem helicase cassettes in Brr2-mediated remodeling of the spliceosome. *Proc. Natl. Acad. Sci. U.S.A.*, **109**, 17418–17423.
22. Galej,W.P., Oubridge,C., Newman,A.J. and Nagai,K. (2013) Crystal structure of Prp8 reveals active site cavity of the spliceosome. *Nature*, **493**, 638–643.
23. Yan,C., Hang,J., Wan,R., Huang,M., Wong,C.C. and Shi,Y. (2015) Structure of a yeast spliceosome at 3.6-angstrom resolution. *Science*, **349**, 1182–1191.
24. Mozaffari-Jovin,S., Wandersleben,T., Santos,K.F., Will,C.L., Luhrmann,R. and Wahl,M.C. (2013) Inhibition of RNA helicase Brr2 by the C-terminal tail of the spliceosomal protein Prp8. *Science*, **341**, 80–84.
25. Mozaffari-Jovin,S., Wandersleben,T., Santos,K.F., Will,C.L., Luhrmann,R. and Wahl,M.C. (2014) Novel regulatory principles of the spliceosomal Brr2 RNA helicase and links to retinal disease in humans. *RNA Biol.*, **11**, 298–312.
26. Theuser,M., Hobartner,C., Wahl,M.C. and Santos,K.F. (2016) Substrate-assisted mechanism of RNP disruption by the spliceosomal Brr2 RNA helicase. *Proc. Natl. Acad. Sci. U.S.A.*, **113**, 7798–7803.
27. van Nues,R.W. and Beggs,J.D. (2001) Functional contacts with a range of splicing proteins suggest a central role for Brr2p in the dynamic control of the order of events in spliceosomes of Saccharomyces cerevisiae. *Genetics*, **157**, 1451–1467.
28. Cordin,O., Hahn,D., Alexander,R., Gautam,A., Saveanu,C., Barrass,J.D. and Beggs,J.D. (2014) Brr2p carboxy-terminal Sec63 domain modulates Prp16 splicing RNA helicase. *Nucleic Acids Res.*, **42**, 13897–13910.
29. Chen,H.C., Tseng,C.K., Tsai,R.T., Chung,C.S. and Cheng,S.C. (2013) Link of NTR-mediated spliceosome disassembly with DEAH-box ATPases Prp2, Prp16, and Prp22. *Mol. Cell. Biol.*, **33**, 514–525.
30. Nguyen,T.H., Galej,W.P., Bai,X.C., Savva,C.G., Newman,A.J., Scheres,S.H. and Nagai,K. (2015) The architecture of the spliceosomal U4/U6.U5 tri-snRNP. *Nature*, **523**, 47–52.
31. Agafonov,D.E., Deckert,J., Wolf,E., Odenwalder,P., Bessonov,S., Will,C.L., Urlaub,H. and Luhrmann,R. (2011) Semiquantitative proteomic analysis of the human spliceosome via a novel two-dimensional gel electrophoresis method. *Mol. Cell. Biol.*, **31**, 2667–2682.
32. Ulrich,A.K., Schulz,J.F., Kamprad,A., Schutze,T. and Wahl,M.C. (2016) Structural basis for the functional coupling of the alternative splicing factors Smu1 and RED. *Structure*, **24**, 762–773.
33. Ulrich,A.K., Seeger,M., Schutze,T., Bartlick,N. and Wahl,M.C. (2016) Scaffolding in the spliceosome via single alpha helices. *Structure*, **24**, 1972–1983.
34. Hegele,A., Kamburov,A., Grossmann,A., Sourlis,C., Wowro,S., Weimann,M., Will,C.L., Pena,V., Luhrmann,R. and Stelzl,U. (2012) Dynamic protein-protein interaction wiring of the human spliceosome. *Mol. Cell*, **45**, 567–580.
35. Fournier,G., Chiang,C., Munier,S., Tomoiu,A., Demeret,C., Vidalain,P.O., Jacob,Y. and Naffakh,N. (2014) Recruitment of RED-SMU1 complex by Influenza A Virus RNA polymerase to control Viral mRNA splicing. *PLoS Pathog.*, **10**, e1004164.
36. Huang,X., Beullens,M., Zhang,J., Zhou,Y., Nicolaescu,E., Lesage,B., Hu,Q., Wu,J., Bollen,M. and Shi,Y. (2009) Structure and function of the two tandem WW domains of the pre-mRNA splicing factor FBP21 (formin-binding protein 21). *J. Biol. Chem.*, **284**, 25375–25387.
37. Klippel,S., Wieczorek,M., Schumann,M., Krause,E., Marg,B., Seidel,T., Meyer,T., Knapp,E.W. and Freund,C. (2011) Multivalent binding of formin-binding protein 21 (FBP21)-tandem-WW domains fosters protein recognition in the pre-spliceosome. *J. Biol. Chem.*, **286**, 38478–38487.
38. Kofler,M., Heuer,K., Zech,T. and Freund,C. (2004) Recognition sequences for the GYF domain reveal a possible spliceosomal function of CD2BP2. *J. Biol. Chem.*, **279**, 28292–28297.
39. Woolard,J., Vousden,W., Moss,S.J., Krishnakumar,A., Gammons,M.V., Nowak,D.G., Dixon,N., Micklefield,J., Spannhoff,A., Bedford,M.T. *et al.* (2011) Borrelidin modulates the alternative splicing of VEGF in favour of anti-angiogenic isoforms. *Chem. Sci.*, **2011**, 273–278.
40. Worseck,J.M., Grossmann,A., Weimann,M., Hegele,A. and Stelzl,U. (2012) A stringent yeast two-hybrid matrix screening approach for protein-protein interaction discovery. *Methods Mol. Biol.*, **812**, 63–87.
41. Mozaffari-Jovin,S., Santos,K.F., Hsiao,H.H., Will,C.L., Urlaub,H., Wahl,M.C. and Luhrmann,R. (2012) The Prp8 RNase H-like domain inhibits Brr2-mediated U4/U6 snRNA unwinding by blocking Brr2 loading onto the U4 snRNA. *Genes Dev.*, **26**, 2422–2434.
42. Yang,B., Wu,Y.J., Zhu,M., Fan,S.B., Lin,J., Zhang,K., Li,S., Chi,H., Li,Y.X., Chen,H.F. *et al.* (2012) Identification of cross-linked peptides from complex samples. *Nat. Methods*, **9**, 904–906.
43. Vranken,W.F., Boucher,W., Stevens,T.J., Fogh,R.H., Pajon,A., Llinas,M., Ulrich,E.L., Markley,J.L., Ionides,J. and Laue,E.D. (2005)

The CCPN data model for NMR spectroscopy: development of a software pipeline. *Proteins*, **59**, 687–696.
44. Han,B., Liu,Y., Ginzinger,S.W. and Wishart,D.S. (2011) SHIFTX2: significantly improved protein chemical shift prediction. *J. Biomol. NMR*, **50**, 43–57.
45. Zhang,D., Jiang,P., Xu,Q. and Zhang,X. (2011) Arginine and glutamate-rich 1 (ARGLU1) interacts with mediator subunit 1 (MED1) and is required for estrogen receptor-mediated gene transcription and breast cancer cell growth. *J. Biol. Chem.*, **286**, 17746–17754.
46. Forch,P. and Valcarcel,J. (2001) Molecular mechanisms of gene expression regulation by the apoptosis-promoting protein TIA-1. *Apoptosis*, **6**, 463–468.
47. Forch,P., Puig,O., Kedersha,N., Martinez,C., Granneman,S., Seraphin,B., Anderson,P. and Valcarcel,J. (2000) The apoptosis-promoting factor TIA-1 is a regulator of alternative pre-mRNA splicing. *Mol. Cell*, **6**, 1089–1098.
48. Forch,P., Puig,O., Martinez,C., Seraphin,B. and Valcarcel,J. (2002) The splicing regulator TIA-1 interacts with U1-C to promote U1 snRNP recruitment to 5' splice sites. *EMBO J.*, **21**, 6882–6892.
49. Izquierdo,J.M. and Valcarcel,J. (2007) Two isoforms of the T-cell intracellular antigen 1 (TIA-1) splicing factor display distinct splicing regulation activities. Control of TIA-1 isoform ratio by TIA-1-related protein. *J. Biol. Chem.*, **282**, 19410–19417.
50. Hocking,H.G., Zangger,K. and Madl,T. (2013) Studying the structure and dynamics of biomolecules by using soluble paramagnetic probes. *Chemphyschem*, **14**, 3082–3094.
51. Lian,L.-Y. and Roberts,G.C.K. (2011) *Protein NMR Spectroscopy: Practical Techniques and Applications*. Wiley, Chichester.
52. Silvestre-Ryan,J., Bertoncini,C.W., Fenwick,R.B., Esteban-Martin,S. and Salvatella,X. (2013) Average conformations determined from PRE data provide high-resolution maps of transient tertiary interactions in disordered proteins. *Biophys. J.*, **104**, 1740–1751.
53. Clore,G.M. and Iwahara,J. (2009) Theory, practice, and applications of paramagnetic relaxation enhancement for the characterization of transient low-population states of biological macromolecules and their complexes. *Chem. Rev.*, **109**, 4108–4139.
54. Bedford,M.T., Reed,R. and Leder,P. (1998) WW domain-mediated interactions reveal a spliceosome-associated protein that binds a third class of proline-rich motif: the proline glycine and methionine-rich motif. *Proc. Natl. Acad. Sci. U.S.A.*, **95**, 10602–10607.
55. Teigelkamp,S., Achsel,T., Mundt,C., Gothel,S.F., Cronshagen,U., Lane,W.S., Marahiel,M. and Luhrmann,R. (1998) The 20kD protein of human [U4/U6.U5] tri-snRNPs is a novel cyclophilin that forms a complex with the U4/U6-specific 60kD and 90kD proteins. *RNA*, **4**, 127–141.
56. Schmidt,C., Gronborg,M., Deckert,J., Bessonov,S., Conrad,T., Luhrmann,R. and Urlaub,H. (2014) Mass spectrometry-based relative quantification of proteins in precatalytic and catalytically active spliceosomes by metabolic labeling (SILAC), chemical labeling (iTRAQ), and label-free spectral count. *RNA*, **20**, 406–420.
57. Chen,C.H., Yu,W.C., Tsao,T.Y., Wang,L.Y., Chen,H.R., Lin,J.Y., Tsai,W.Y. and Cheng,S.C. (2002) Functional and physical interactions between components of the Prp19p-associated complex. *Nucleic Acids Res.*, **30**, 1029–1037.
58. Makarova,O.V., Makarov,E.M., Urlaub,H., Will,C.L., Gentzel,M., Wilm,M. and Luhrmann,R. (2004) A subset of human 35S U5 proteins, including Prp19, function prior to catalytic step 1 of splicing. *EMBO J.*, **23**, 2381–2391.
59. Bessonov,S., Anokhina,M., Krasauskas,A., Golas,M.M., Sander,B., Will,C.L., Urlaub,H., Stark,H. and Luhrmann,R. (2010) Characterization of purified human Bact spliceosomal complexes reveals compositional and morphological changes during spliceosome activation and first step catalysis. *RNA*, **16**, 2384–2403.
60. Sharma,R., Raduly,Z., Miskei,M. and Fuxreiter,M. (2015) Fuzzy complexes: Specific binding without complete folding. *FEBS Lett.*, **589**, 2533–2542.
61. Tsai,R.T., Tseng,C.K., Lee,P.J., Chen,H.C., Fu,R.H., Chang,K.J., Yeh,F.L. and Cheng,S.C. (2007) Dynamic interactions of Ntr1-Ntr2 with Prp43 and with U5 govern the recruitment of Prp43 to mediate spliceosome disassembly. *Mol. Cell. Biol.*, **27**, 8027–8037.
62. Wan,R., Yan,C., Bai,R., Wang,L., Huang,M., Wong,C.C. and Shi,Y. (2016) The 3.8 A structure of the U4/U6.U5 tri-snRNP: Insights into spliceosome assembly and catalysis. *Science*, **351**, 466–475.
63. Agafonov,D.E., Kastner,B., Dybkov,O., Hofele,R.V., Liu,W.T., Urlaub,H., Luhrmann,R. and Stark,H. (2016) Molecular architecture of the human U4/U6.U5 tri-snRNP. *Science*, **351**, 1416–1420.